ACS OMEGA

Open Access

http://pubs.acs.org/journal/acsodf

Article

Effect of Aspect Ratio of a Gold-Nanorod-Modified Screen-Printed Carbon Electrode for Carbaryl Detection in Three Different Samples of Vegetables

Wulan Tri Wahyuni,* Budi Riza Putra, Hemas Arif Rahman, Tribidasari A. Ivandini, Irkham, Munawar Khalil, and Isnaini Rahmawati

Cite This: *ACS Omega* 2024, 9, 1497−1515

Read Online

ACCESS | Metrics & More | Article Recommendations

ABSTRACT: In this study, three different sizes of gold nanorods (AuNRs) were synthesized using the seed-growth method by adding various volumes of $AgNO_3$ as 400, 600, and 800 μL into the growth solution of gold nanoparticles. Three different sizes of AuNRs were then characterized using UV−vis spectroscopy, high-resolution transmission electron microscopy (HRTEM), selected area electron diffraction (SAED) patterns, and atomic force microscopy (AFM) to investigate the surface morphology, topography, and aspect ratios of each synthesized AuNR. The aspect ratios from the histogram of size distributions of three AuNRs as 2.21, 2.53, and 2.85 can be calculated corresponding to the addition of $AgNO_3$ volumes of 400, 600, and 800 μL. Moreover, each AuNR in three different aspect ratios was drop-cast onto the surface of a commercial screen-printed carbon electrode (SPCE) to obtain three different SPCE-modified AuNRs (SPCE-A400, SPCE-A600, and SPCE-A800, respectively). All SPCE-modified AuNRs were then evaluated for their electrochemical behavior using cyclic voltammetry and electrochemical impedance spectroscopy (EIS) techniques and the highest electrochemical performance was shown as the order of magnitude of SPCE-A400 > SPCE-A600/SPCE-A800. The reason for the highest electrocatalytic activity of SPCE-A400 might be due to the smallest particle size and uniform distribution of AuNRs ∼ 2.2, which enhanced the charge transfer, thus providing the highest electroactive surface area (0.6685 cm^2) compared to other electrodes. These results also confirm that the sensing mechanism for all SPCE-modified AuNRs is controlled by diffusion phenomena. In addition, the optimum pH was obtained as 4 for carbaryl detection for all SPCE-modified AuNRs with the highest current shown by SPCE-A400. Furthermore, SPCE-A400 has the highest fundamental parameters (surface coverage, catalytic rate constant, electron transfer rate constant, and adsorption capacity) for carbaryl detection, which were investigated using cyclic voltammetry and chronoamperometric techniques. The electroanalytical performances of all SPCE-modified AuNRs for carbaryl detection were also investigated with SPCE-A400 displaying the best performance among other electrodes in terms of its linearity (0.2−100 μM), limit of detection (LOD) ∼ 0.07 μM, and limit of quantification (LOQ) ∼ 0.2 μM. All SPCE-modified AuNRs were also subsequently evaluated for their stability, reproducibility, and selectivity in the presence of interfering species such as $NaNO_2$, NH_4NO_3, $Zn(CH_3CO_2)_2$, $FeSO_4$, diazinon, and glucose and show reliable results as depicted from %RSD values less than 3%. At last, all SPCE-modified AuNRs have been employed for carbaryl detection using a standard addition technique in three different samples of vegetables (cabbage, cucumber, and Chinese cabbage) with its results (%recovery ≈ 100%) within the acceptable analytical range. In conclusion, this work demonstrates the great potential of a disposable device based on an AuNR-modified SPCE for rapid detection and high sensitivity in monitoring the concentration of carbaryl as a residual pesticide in vegetable samples.

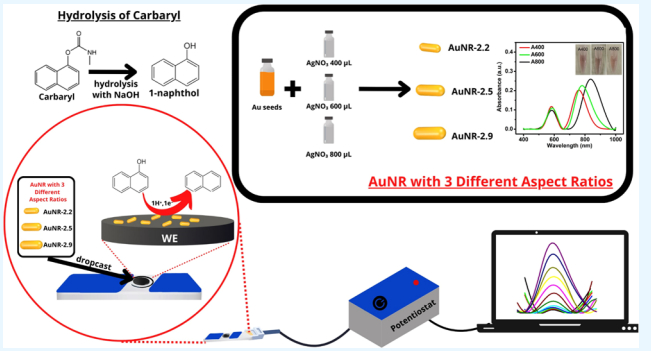

INTRODUCTION

One of the major challenges to ensuring food security for global consumers in the world is the development of rapid detection techniques for detecting pesticide residues and their metabolites in foodstuffs.[1,2] Their bioaccumulation in agricultural land that is highly dangerous for human health may be derived from unregulated and excessive usage and thus adversely impact the quality and safety of foodstuffs.[3,4]

Received: October 10, 2023
Revised: November 24, 2023
Accepted: December 1, 2023
Published: December 19, 2023

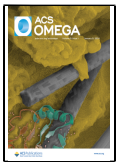

Therefore, developing a robust analytical method for detecting residual pesticides in foodstuffs and monitoring their concentration in the environment is necessary. Among those residual pesticides commonly found in foodstuffs, carbaryl as a carbamate family has been widely used to increase production in agricultural lands due to its high efficiency and powerful activity in controlling the population of harmful insects to a variety of plant crops.[5,6] When the carbaryl residue occurs in food and subsequently enters the human body, it can cause a great threat and lead to several serious failures and hazards in the metabolic system.[7−9] Moreover, the European Union (EU) has regulated the maximum residue limits (MRLs) of carbaryl concentration in several foodstuffs from 0.01 to 0.05 mg kg^{-1}.[10] Meanwhile, the United States Environmental Protection Agency (US EPA) has established the MRLs for cabbage, leafy, and root vegetables at 21, 10, and 75 mg kg^{-1}, respectively.[11] In addition, the acceptable daily intake (ADI) of carbaryl for humans is 0.01 mg kg^{-1} body weight per day.[12] As a result, there is a critical need to develop a portable and reliable analytical method for the quantification of residual carbaryl concentrations in food matrices for food safety assessment and environmental pollution monitoring.

There are several analytical methods based on instrumentation techniques that have been developed to quantify the residual carbaryl concentrations in various matrices, such as high-performance liquid chromatography (HPLC),[13,14] HPLC mass spectrometry,[15−17] supercritical fluid chromatography-mass spectrometry (SFC-MS),[18] gas chromatography-mass spectrometry (GC-MS),[19,20] surface-enhanced Raman spectroscopy (SERS),[21,22] infrared spectroscopy,[23] colorimetry,[24,25] fluorescence,[26,27] enzyme-linked immunosorbent assay (ELISA),[28,29] and electrochemical methods.[30−32] Most of these analytical techniques for carbaryl detection possess unavoidable drawbacks such as complex processes for sample pretreatment, time-consuming, employment of specific reagents, and sophisticated instruments that cannot meet the requirements to be further developed for onsite pesticide detection.[33−35] Therefore, developing a portable analytical method for the rapid detection of carbaryl residues in food matrices is urgently needed for practical applications.

In contrast, electrochemical methods based on a disposable screen-printed carbon electrode (SPCE) offer an excellent alternative option for onsite pesticide detection owing to their rapid, low-cost, simple operation, versatility, and high sensitivity.[36−38] Meanwhile, the employment of different shapes of gold nanoparticles via nanospheres,[39−41] nanorods,[42−44] nanocubes,[45−47] nanostars,[48−50] nanocages,[51−53] nanotriangles,[54−56] nanohexagon,[57−59] and nanobipyramids[60−62] has been widely explored to enhance its sensitivity for the purpose of sensing applications. Among these various shapes of gold nanoparticles, gold nanorods (AuNRs) have attracted considerable attention due to their anisotropic structures and high surface area that could facilitate faster electron transfer capability on the electrode surface.[63] In addition, the presence of AuNRs on the surface of SPCE could improve the sensitivity of the electrochemical sensor by adjusting the aspect ratio (length/diameter) of nanorods during the synthesis of gold nanoparticles.[64] One way to control the aspect ratio of the synthesized AuNRs is by varying the added amount of silver nitrate as a specific directing agent into the growth solution of gold nanoparticles to achieve different size dimensions of individual particles of gold nanorods.[65,66] The utilization of gold nanorods and their composites to modify the electrode surface has been reported for the detection of several electroactive molecules such as dopamine,[67,68] glucose,[69] hydrogen peroxide,[70] redox protein,[71−73] dyes,[74,75] and bacteria.[76,77]

However, to the best of our knowledge, we here describe the first systematic investigation of an electrochemical sensor based on three different aspect ratios of gold nanorods modified on commercial SPCE for carbaryl detection. It is expected that the smallest aspect ratio of AuNRs will provide the highest electrocatalytic activity toward carbaryl oxidation on the electrode surface. The developed sensors based on three different aspect ratios of AuNR-modified SPCE were comprehensively investigated from the very beginning of the experiments to optimize each analytical performance toward carbaryl detection and further employed in three different samples of vegetables.

EXPERIMENTAL SECTION

Materials. Commercial screen-printed carbon electrodes (SPCE) DS-110 were obtained from DS Dropsens, Spain. All chemicals used in this study were used as received without further purification, such as $HAuCl_4$, cetyltrimethylammonium bromide (CTAB), $AgNO_3$, $NaBH_4$, NaH_2PO_4, H_3PO_4, $NaNO_2$, $FeSO_4$, $Zn(CH_3CO_2)_2$, NH_4NO_3, HCl, NaOH, ascorbic acid, diazinon, and glucose. Carbaryl (CAS: 63-25-2, purity > 98%) was obtained from Tokyo Chemical Industry (TCI) Co. Ltd. Deionized water was used in the whole experiment.

Instrumentation. A Palmens Emstat 3+ (ES316U669) device running PS Trace 5.9 software was used for the electrochemical studies. Meanwhile, a PalmSens 4.0 Potentiostat/Galvanostat/Impedance Analyzer (Palm Sens Compact Electrochemical Interfaces, The Netherlands) was employed to perform electrochemical impedance spectroscopy (EIS) studies. All electrochemical experiments were conducted at an ambient temperature (25 ± 2 °C). UV−vis absorption spectra from three synthesized AuNRs were measured using a UV−visible Spectrophotometer M51 Bel Engineering. The morphology of the synthesized AuNRs was characterized by using scanning transmission electron microscopy (Talos F200X G2 TEM) under a working voltage of 200 kV. The surface topography of SPCE-modified AuNR was characterized by atomic force microscopy (Park System NX 10 AFM). Standard laboratory equipment such as Eppendorf micropipettes, Pyrex glassware, analytical balance, and ovens were employed to assist solution preparation.

METHODS

Synthesis of a Gold Nanorod (AuNR) and Its Electrode Preparation. Both seeds and growth solutions are required for the preparation process of the gold nanorod (AuNR) synthesis. The seed solution was prepared by mixing 10 mL of 0.5 mM $HAuCl_4$ with 10 mL of 0.2 M CTAB and slowly stirring for 5 min. The obtained solution was left for 10 min and mixed with 1.2 mL of 0.01 M $NaBH_4$. The color of the solution will change from yellow to brown and the stirring must be stopped for approximately 2 min. The seed solution should be left for 2 h before it was used for AuNR synthesis. All experimental conditions must be maintained at a temperature of 25−30 °C. Meanwhile, the growth solution was prepared by adding 10 mL of 0.25 mM $HAuCl_4$ with 10 mL of 0.2 M CTAB and slowly stirring for 5 min. The solution

https://doi.org/10.1021/acsomega.3c07831
ACS Omega 2024, 9, 1497−1515

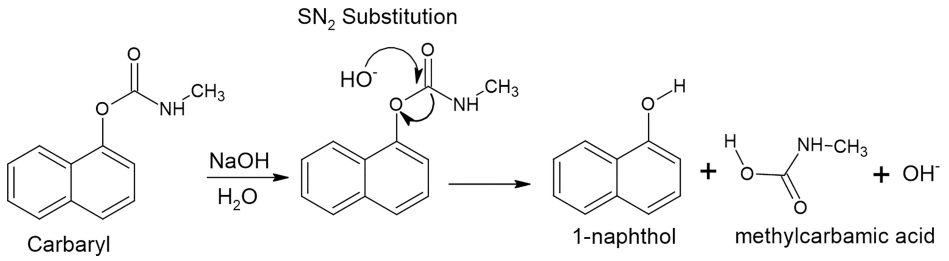

Figure 1. Schematic illustration of the hydrolysis of carbaryl into 1-naphthol in alkaline conditions.

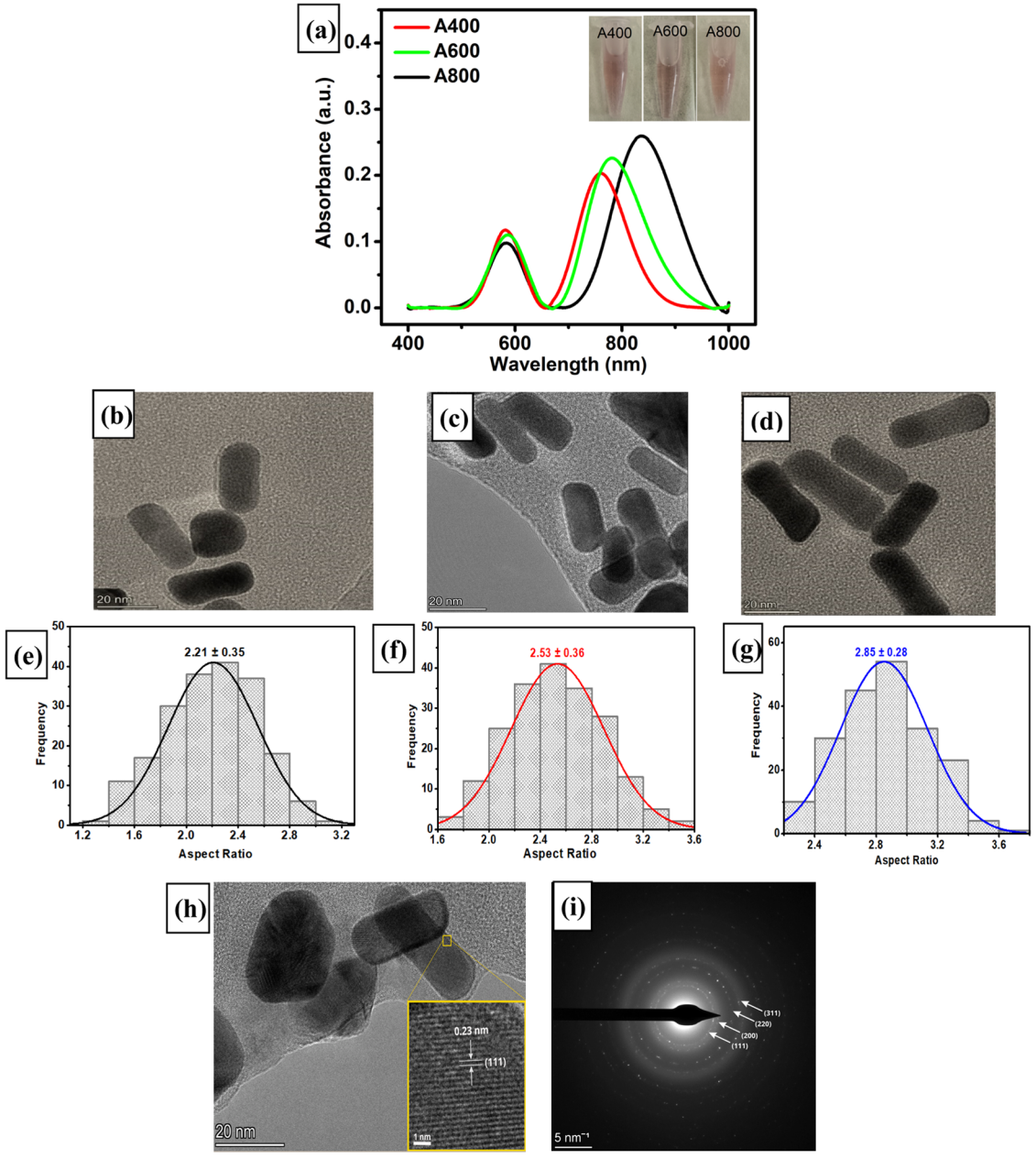

Figure 2. (a) UV−vis spectra of AuNR in three different aspect ratios. TEM images of three synthesized AuNRs in three different aspect ratios (b) A400, (c) A600, and (d) A800, and (e−g) their corresponding histograms of size distribution. (h) High-resolution transmission electron microscopy (HRTEM) image and (i) selected area electron diffraction (SAED) pattern of AuNR.

was left for 10 min and 140 μL of 0.0788 M ascorbic acid was added. Then, different volumes of 4 mM $AgNO_3$ (400, 600, and 800 μL) were added to the growth solution. The resulting growth solution of AuNR is labeled as A400, A600, and A800, corresponding to the addition of 400, 600, and 800 μL of $AgNO_3$. Each growth solution was then subsequently added with 300 μL of 1 M HCl and 24 μL of seed solution. The obtained solution was left for 72 h at a temperature of 30 °C.

https://doi.org/10.1021/acsomega.3c07831
ACS Omega 2024, 9, 1497−1515

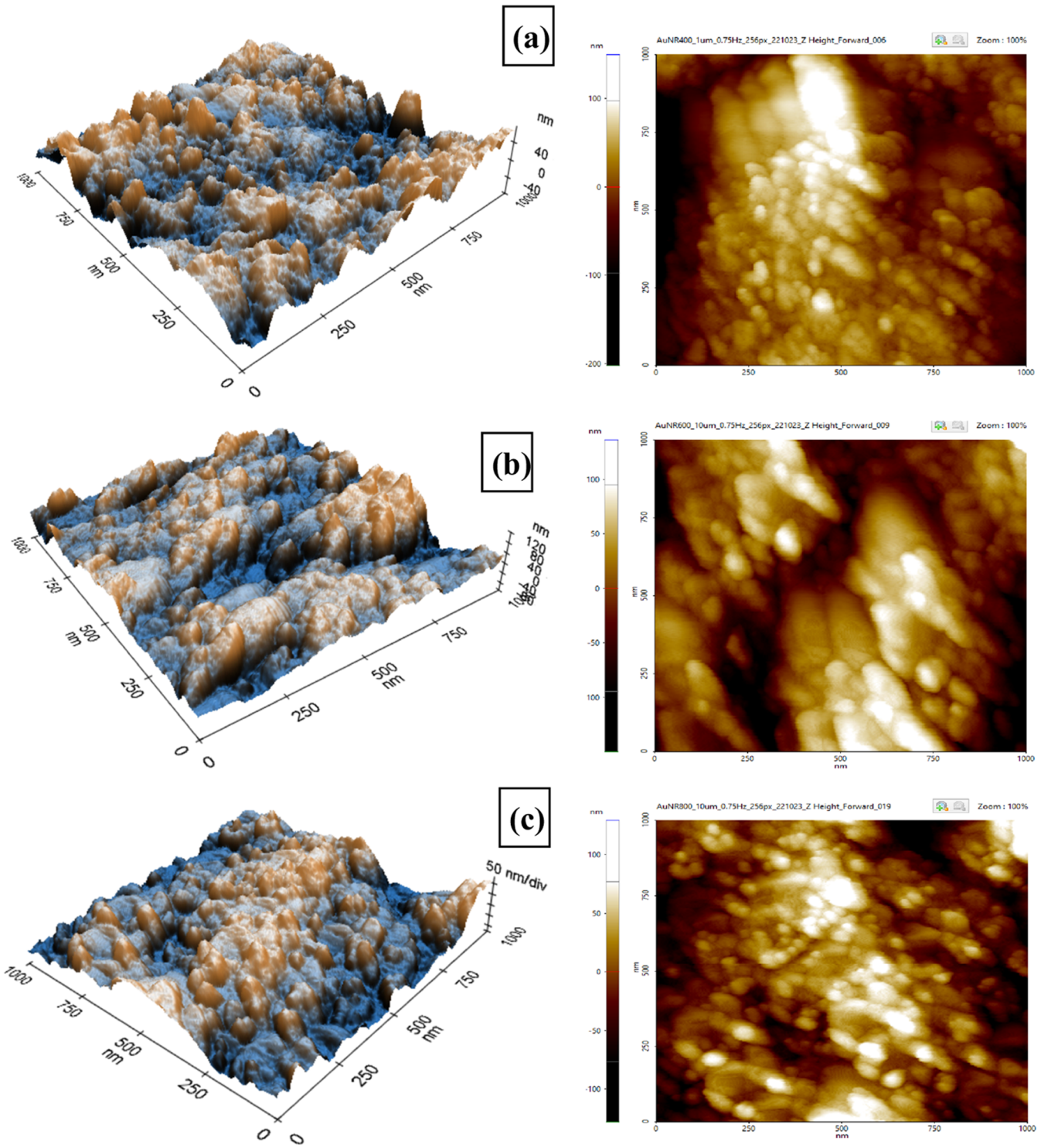

Figure 3. AFM image in 3D topographical dimension (left) and AFM height image (right) of the synthesized AuNRs with three different aspect ratios for (a) A400, (b) A600, and (c) A800.

The final solution containing AuNR in different particle sizes was separated from its filtrate by the centrifugation process. Then, each 4 μL of AuNR solution labeled as A400, A600, and A800 was drop-casted onto the surface of the SPCE and then dried in an oven at 100 °C for 5 min.

Preparation of Carbaryl and Phosphate Buffer Solution. Prior to measurement, the carbaryl solution should be hydrolyzed in an alkaline condition by converting it into 1-naphthol following the mechanism of SN_2 substitution,[78,79] as illustrated in Figure 1. The hydrolysis of carbaryl into 1-naphthol was performed by dissolving 0.022 g of carbaryl to obtain its concentration as 1 mM in 100 mL of 0.1 M NaOH. The stock solution of 1 mM carbaryl was then heated to 70 °C with stirring conditions for 30 min. Meanwhile, a phosphate buffer solution was prepared by dissolving appropriate amounts of H_3PO_4 and NaH_2PO_4 in deionized water to adjust the pH to 4.

https://doi.org/10.1021/acsomega.3c07831
ACS Omega 2024, 9, 1497−1515

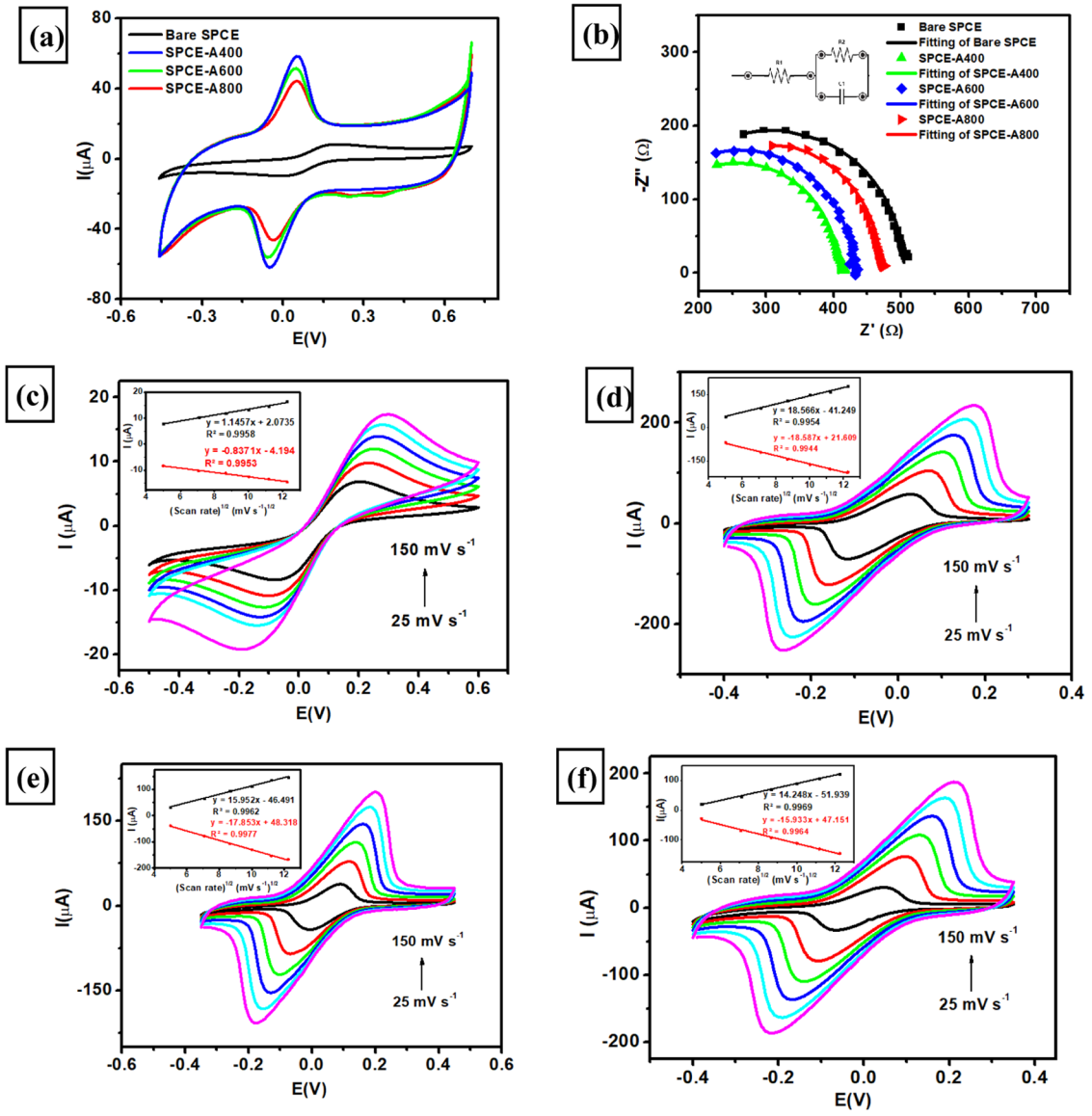

Figure 4. (a) Cyclic voltammograms obtained at a scan rate 50 mV s^{-1}, (b) Nyquist plot for the measurements of 1 mM $K_3[Fe(CN)_6]$ in 0.1 M KCl using four different electrodes at a frequency range from 10^6 to 10^2 Hz, E_{dc} = 0 V, and E_{ac} = 10 mV, cyclic voltammogram obtained at various scan rates (25−150 mV s^{-1}) for the measurements of 1 mM $K_3[Fe(CN)_6]$ in 0.1 M KCl using (c) bare SPCE, (d) SPCE-A400, (e) SPCE-A600, and (f) SPCE-A800.

Linearity, Limit of Detection (LOD), and Limit of Quantification (LOQ). Linearity was evaluated by measuring the carbaryl solution in a concentration range of 0.2−100 μM in 0.1 M phosphate buffer of pH 7 using SPCE-modified AuNR in three different aspect ratios. The concentrations of carbaryls were determined using differential pulse voltammetry (DPV) and amperometry. DPV was performed in the potential range from −0.2 to 0.6 V with a scan rate of 50 mV s^{-1} in triplicates. Amperometry was performed at a potential of 0.48 V with a $t_{interval}$ of 0.1 s and $t_{running}$ of 20 s. From the measurement of carbaryl in the concentration range of 0.2−100 μM in triplicate, three calibration curves were obtained with its determination coefficient (R^2). DPV and amperometry techniques were selected for further investigation of carbaryl measurements, as they provide the highest sensitivity, as indicated by $R^2 \approx 1$. Linearity was evaluated from the relationship between the concentration of the solution and the current response of carbaryl measurements. The limit of detection (LOD) was calculated based on the signal-to-noise (S/N) ratio by gradually decreasing the carbaryl concentration until the ratio of S/N was obtained as 3:1. Meanwhile, the limit of quantification (LOQ) was estimated from the LOD value multiplied by three.

Reproducibility, Stability, and Selectivity. Reproducibility was evaluated by preparing six different electrodes of SPCE-modified AuNR with different aspect ratios (A400, A600, and A800). The electrodes were then employed using measurements of 100 μM carbaryl solution in 0.1 M phosphate buffer of pH 4. The evaluation of electrode stability was also performed by measuring 100 μM carbaryl solution in 0.1 M phosphate buffer at pH 4 using the same electrode for 4 consecutive days. The study of sensor selectivity was performed by measuring 100 μM carbaryl solution in the presence of sodium nitrite, ammonium nitrite, zinc acetate, iron sulfate, diazinon, and glucose as interfering agents, prepared from a 100 μM standard solution and dissolved in

https://doi.org/10.1021/acsomega.3c07831
ACS Omega 2024, 9, 1497−1515

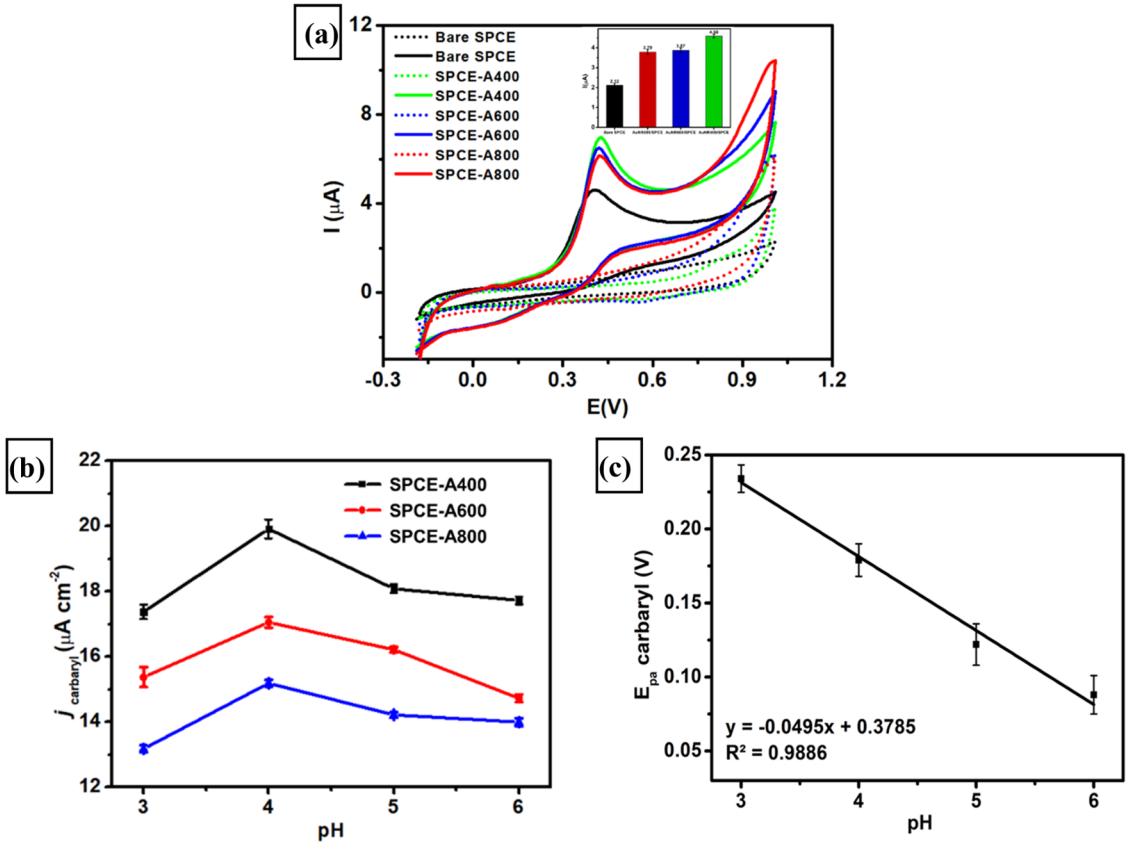

Figure 5. (a) Cyclic voltammogram and inset is the corresponding bar chart diagram of peak current of 0.1 M phosphate buffer of pH 4 containing 100 μM carbaryl using bare SPCE, SPCE-A400, SPCE-A600, and SPCE-AuNR800, (b) plots of peak current vs the pH value, and (c) linear relationship between peak current of carbaryl oxidation with its pH solution measured from 100 μM carbaryl in 0.1 M phosphate buffer in various pH values (3−6) in SPCE-A400.

0.1 M phosphate buffer of pH 4. Before and after the addition of interfering agents, the carbaryl solution was measured three times by using the differential pulse voltammetry technique. All electrochemical measurements were performed using differential pulse voltammetry, at a potential range from −0.2 to 0.6 V, at a scan rate of 50 mV s^{-1}, a potential step of 10 mV, a potential pulse of 50 mV, and a pulse time of 50 ms.

Sample Preparation for Real Analysis. The determination of carbaryl in real samples was conducted using the standard addition technique. Cabbage was employed as a real sample that was purchased from the local market in Bogor, West Java, Indonesia. Ten grams of cabbage sample was extracted with 25 mL of 0.1 M NaOH followed by sonication for 40 min. Then, the obtained solution was filtered to obtain its filtrate after the filtration process. The filtrate was subsequently hydrolyzed with heat treatment at 70 °C followed by vigorous stirring for 30 min. The resulting filtrate after the hydrolysis process was collected, and 2 mL of its solution was spiked with carbaryl standard solution in the concentration range from 10 to 50 μM diluted in 0.1 M phosphate buffer of pH 4. The measurement of carbaryl in cabbage samples was performed using the DPV technique using three modified electrodes (SPCE-A400, SPCE-A600, SPCE-A800) at an oxidation potential of 0.2 V.

RESULTS AND DISCUSSION

Characterization of Synthesized AuNRs with Different Amounts of $AgNO_3$ Using UV−Vis Spectroscopy, TEM, SEM, and AFM Techniques. UV−vis spectroscopy is one of the most widely used techniques for characterizing the optical properties and electronic structure of three synthesized gold nanorods (AuNRs) as their absorption bands could be related to the aspect ratio of metal nanoparticles. Based on Figure 2, the colloidal solutions of three synthesized AuNRs show a distinctive purple color that arises from their tiny dimensions of nanoparticles. It has been known that the synthesized AuNRs possess two characteristic bands of plasmon resonance that are related to their axis dimension at 560 nm (width) and 750 nm (length) of the nanorod.[80,81] Thus, it can be expected that the changes in absorption intensity of these two bands will be strongly influenced by the aspect ratio of the synthesized AuNRs particularly in their 2D dimension of length and width, as shown in Figure 2a. Based on this figure, it is clear that the absorption intensity at their longitudinal band (750 nm) increased and slightly shifted to a higher wavelength when more $AgNO_3$ was added to the AuNR solution while the intensity in the transverse band (560 nm) slightly diminished. According to this result, one of the key factors to obtain AuNRs with different lengths is by adding an increasing concentration of $AgNO_3$ to the solution of Au seeds. The solution containing Au seeds can be considered as nuclear for the anisotropic growth of AuNRs in all directions by adding different amounts of $AgNO_3$. Therefore, it makes sense from the result of three synthesized AuNRs that the length of nanoparticles will increase when a higher amount of $AgNO_3$ is added to the gold solution, and only small changes are observed in its width dimension. The exact determination of three synthesized AuNRs in terms of their dimension and

https://doi.org/10.1021/acsomega.3c07831
ACS Omega 2024, 9, 1497−1515

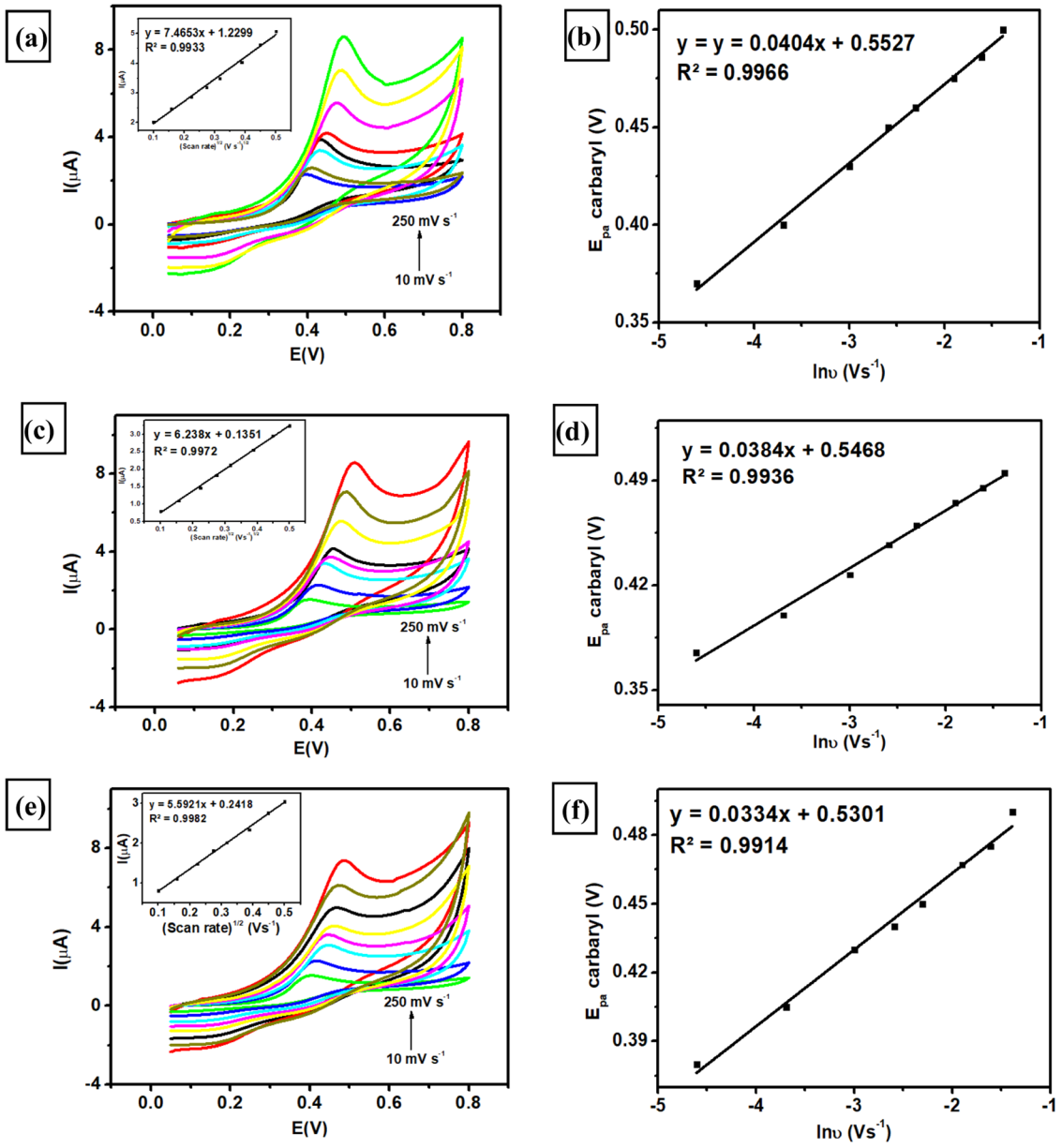

Figure 6. (a, c, e) Voltammograms at various scan rates (10−250 mV s^{-1}) were obtained from the measurement of 100 μM carbaryl in 0.1 M phosphate buffer of pH 4 using three modified electrodes (SPCE-A400, SPCE-A600, and SPCE-A800) and (b, d, f) corresponding linear plot between the natural logarithm of the scan rates (ln v) versus the anodic peak potential (E_{pa}) of carbaryl oxidation.

surface morphology will be further characterized using instrumental techniques such as TEM and AFM.

The morphologies of three synthesized AuNRs were investigated by using transmission electron microscopy (TEM) and size distribution measurements to confirm that the aspect ratio of AuNRs increased with increasing $AgNO_3$ volume. The morphologies of three synthesized AuNRs with different amounts of $AgNO_3$ addition can be observed in Figure 2b−d. It can be seen from these three figures that AuNRs with different sizes were well-dispersed in the as-synthesized solution. In addition, the aspect ratios of three average-sized AuNR samples were 2.21 (29.85 nm in length and 13.52 nm in width) for A400, 2.53 (32.15 nm in length and 12.69 nm in width) for A600, and 2.85 (40.18 nm in length and 14.10 nm in width) for A800, as shown in Figure 2e−g. From this analysis, it is clear that the width of AuNR is almost similar, while its length gradually increased from 29.85 to 40.18 nm.

From the literature, there are three main mechanisms to explain the seed-mediated growth of nonspherical AuNR particles assisted by $AgNO_3$ for controlling its aspect ratio.[82] First, deposition of silver metal onto the longitudinal facets of AuNR under-potential deposition (UPD) condition favors anisotropic growth of the crystal structure.[83] Second, the formation of the CTA−Br−Ag^+ micelle complex on the longitudinal facets of AuNR acts as a capping agent with a synergistic effect from silver to form a soft template by preferentially blocking the growth of AuNR particles.[84,85] Third, this complex has a role in adjusting the orientation of CTAB micelles as a soft template from spherical into cylindrical shapes.[86,87] In our case, the variation of $AgNO_3$ addition into the growth of the AuNR solution was intended to make longer nanorods as well as to enhance its yield. By adding

https://doi.org/10.1021/acsomega.3c07831
ACS Omega 2024, 9, 1497−1515

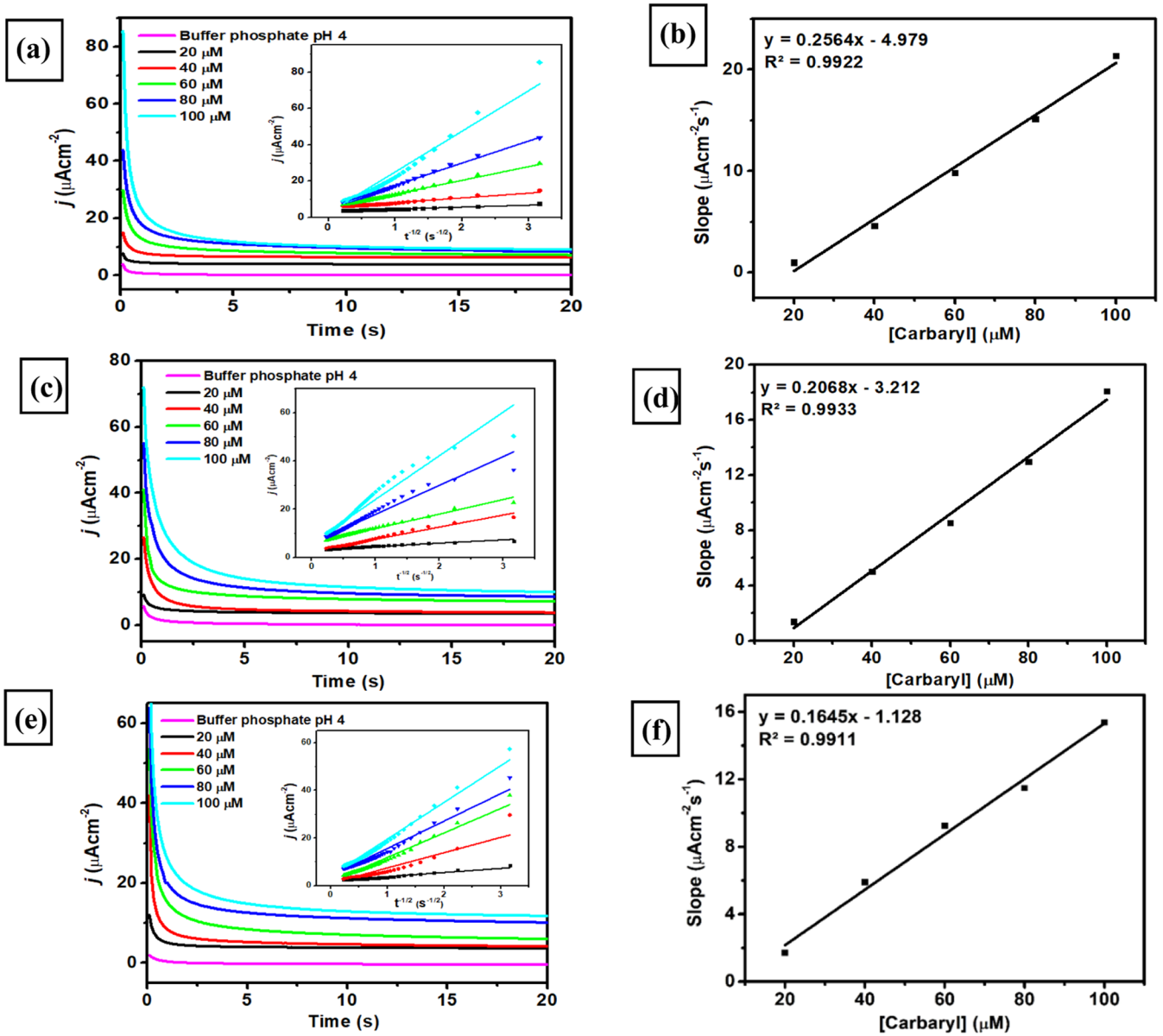

Figure 7. Amperograms obtained from the measurements of carbaryl in the concentration range from 20 to 100 μM in 0.1 M phosphate buffer of pH 4 at the applied potential (E_{dc}) of 0.2 V using (a) SPCE-A400, (c) SPCE-A600, and (e) SPCE-A800; inset: Cotrell plot was taken from each figure. The corresponding calibration plot of carbaryl concentration versus their slopes obtained from the Cotrell plot measured with (b) SPCE-A400, (d) SPCE-A600, and (f) SPCE-A800.

more $AgNO_3$ to create the CTA−Br−Ag^+ complex in AuNR solution, the growth of nanorods is preferentially in the longitudinal rather than in the transverse facets in its crystal structure. Therefore, it is expected that the increasing amount of $AgNO_3$ added to the growth solution will lead to the increased aspect ratios of synthesized AuNR. Further HRTEM analysis confirms that AuNR particles are nearly monodisperse and highly crystalline. The interplanar distance of a single AuNR is 0.23 nm with the growth of nanorods occurring along the (111) plane as shown in Figure 2h. Thus, the selected area electron diffraction (SAED) pattern reveals the characteristics of several interplanar distances for gold with the corresponding planes as follows: 0.23 (111), 0.20 (200), 0.14 (220), and 0.12 nm (311) as shown in Figure 2i.

Atomic force microscopy was used to characterize the surface morphologies of SPCE modified with AuNR in three different aspect ratios (2.21, 2.53, and 2.85) in terms of surface roughness. The surface morphology of the modified electrodes was investigated with a scan area of 1 μm × 1 μm as shown in Figure 3. The AFM image on the left side is topographical in a three-dimensional structure, while the height image and its histogram are on the right side. It can be seen from all topographical AFM images in the three-dimensional (3D) structure of SPCE-modified AuNR are relatively rough with a yellow region that might be from the aggregation of AuNR particles on the surface of SPCE. Based on the analysis of the AFM height image on the right side, a root-mean-square roughness (R_q) value of SPCE-modified A400 is 57 nm (Figure 3a) compared to A600 as 41 nm (Figure 3b) and A800 as 33 nm (Figure 3c). In addition, the peak-to-valley ratio of the line (R_{pv}) provides the highest value at A400 (260 nm) compared to A600 (166 nm) and A800 (153 nm). These results indicate that the smaller aspect ratio of AuNR tends to increase the surface area of the modified electrode more effectively than the

https://doi.org/10.1021/acsomega.3c07831
ACS Omega 2024, 9, 1497−1515

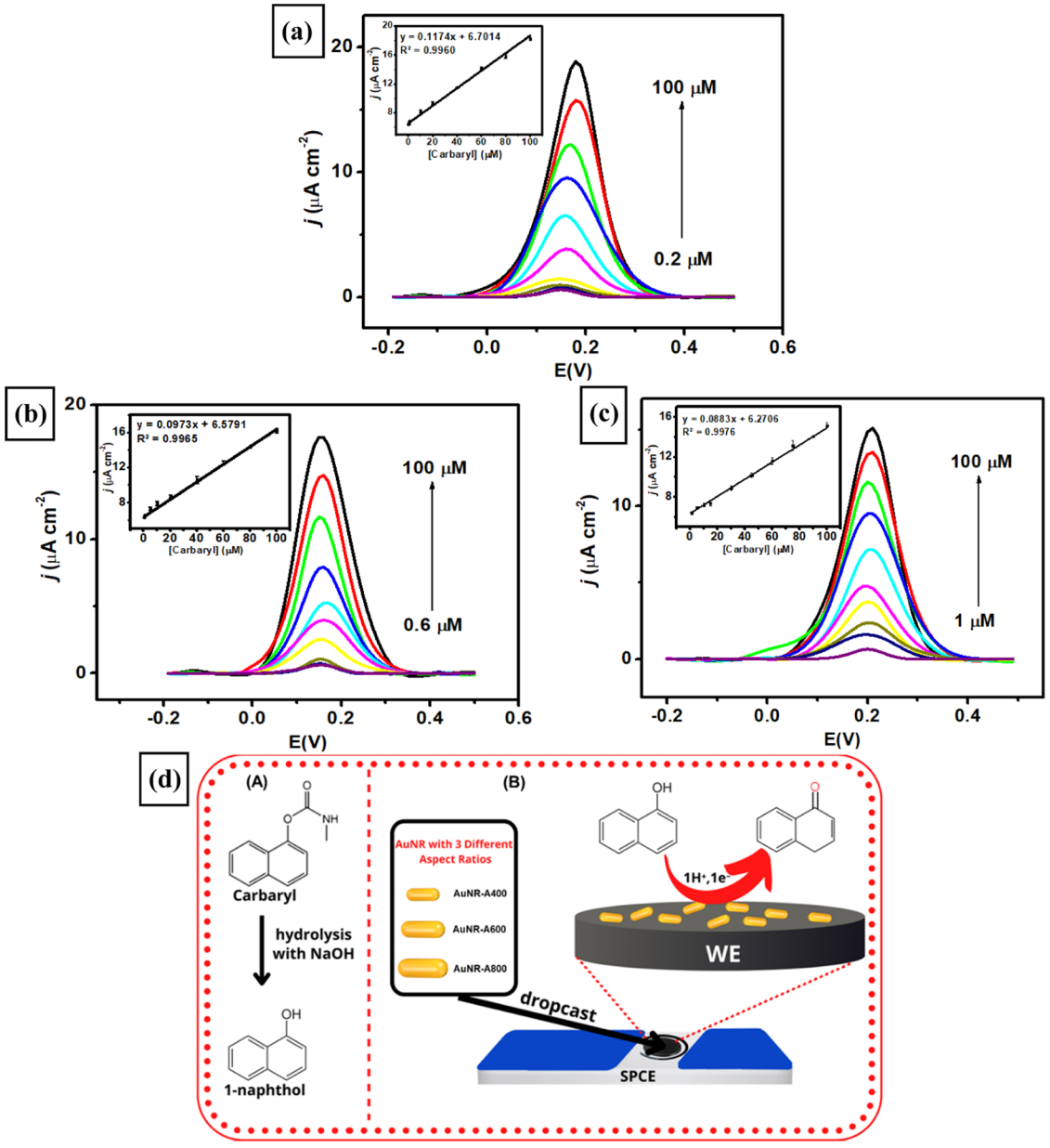

Figure 8. Voltammograms at a scan rate of 50 mV s^{-1} obtained from the measurements of 0.1 M pH 4 phosphate buffer containing different concentrations of carbaryl employing (a) SPCE-A400, (b) SPCE-A600, and (c) SPCE-A800. Inset image: the corresponding calibration plot between the peak current intensity versus different concentrations of carbaryl, (d) schematic illustration of panel (A) hydrolysis reaction from carbaryl into 1-naphthol and (B) mechanism of electrochemical sensing performance based on SPCE-modified AuNR with three different aspect ratios by 1-naphthol oxidation.

higher aspect ratio of nanoparticles. In contrast, the higher aspect ratio of AuNR tends to form large aggregates and cannot properly fill the valleys between the peak region thus resulting in an irregular distribution of nanoparticles on the electrode surface. Therefore, it can be concluded that a smaller particle size of AuNR corresponds to a higher effective surface area due to the high surface-to-volume ratio and may have the potency to effectively enhance its electrochemical performance as a platform for carbaryl detection. Similar phenomenon was also reported in ref 88 which reported a smaller size of Mn_3O_4 nanoparticles exhibited excellent electrocatalytic activity as an electrochemical sensing platform for antibiotic drugs.

Electrochemical Characteristics of Three Types of SPCE-Modified AuNRs in Variation of Their Aspect Ratios. The electrode conductivity was investigated by using CV and EIS techniques by measuring 1 mM $K_3[Fe(CN)_6]$ in 0.1 M KCl with the purpose of investigating the electrochemical performance of SPCE-modified AuNR in different aspect ratios for carbaryl detection. Figure 4a displays the cyclic voltammogram at a scan rate of 50 mV s^{-1} of four different modified electrodes (bare SPCE, SPCE-A400, SPCE-A600, and SPCE-A600) resulting in well-resolved peaks of redox pair for $[Fe(CN)_6]^{3-/4-}$ species. It can be seen from this figure that all three modified electrodes display a significant increase in the current response for both oxidation and reduction processes, corresponding to the reversible electron transfer of Fe^{3+} to Fe^{4+} compared to bare SPCE. In addition, the difference between the oxidation and reduction potentials (ΔE) of $[Fe(CN)_6]^{3-/4-}$ species shown in all SPCE-modified AuNRs is smaller than that observed in bare SPCE, indicating

https://doi.org/10.1021/acsomega.3c07831
ACS Omega 2024, 9, 1497−1515

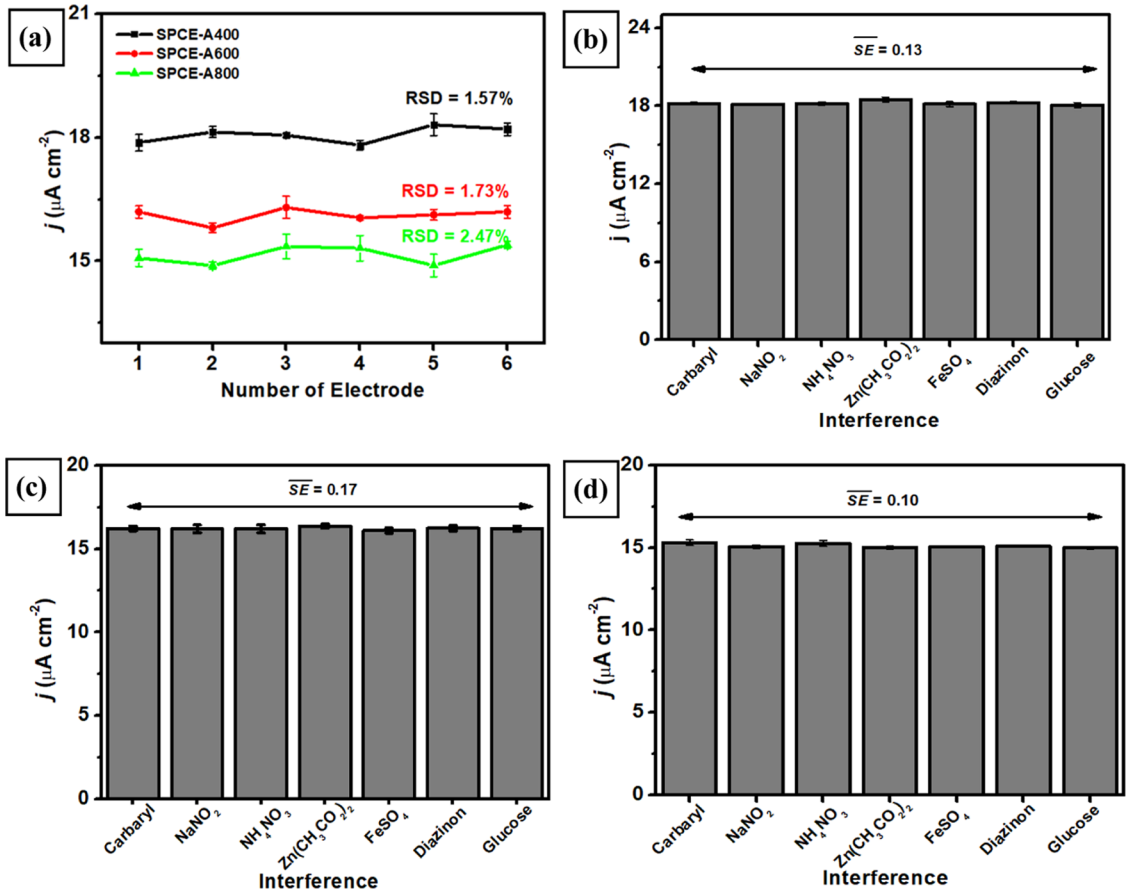

Figure 9. (a) Reproducibility of carbaryl measurements at a concentration of 100 μM carbaryl in 0.1 M phosphate buffer of pH 4 using SPCE-A400, SPCE-A600, and SPCE-A600. Variation in the response current in the measurements of 0.1 M phosphate buffer of pH 4 containing 100 μM carbaryl in the presence of several interferences with a concentration ratio of (1:1) when measured with (b) SPCE-A400, (c) SPCE-A600, and (d) SPCE-A800.

a faster electron transfer process and thus resulting in a higher conductivity of modified electrodes. Among all modified electrodes, SPCE-A400 exhibited the highest current response of oxidation and reduction peak, suggesting a smaller particle of AuNRs, and its particle size distribution greatly influences the electrode conductivity. The trend of the current response of anodic and cathodic peaks was found to be SPCE-A400 > SPCE-A600 > SPCE-A800 > bare SPCE, suggesting that SPCE-A400 assures a better electrochemical performance detection than other electrodes, particularly for carbaryl detection.

Electrochemical impedance spectroscopy (EIS) is a powerful technique to characterize electrode conductivity by investigating charge transfer resistance and interface properties of four different electrodes. Nyquist plots of bare SPCE, SPCE-A400, SPCE-A600, and SPCE-A800 as shown in Figure 4b were obtained by measuring 1 mM $K_3[Fe(CN)_6]$ in 0.1 M KCl in the frequency range of 10^3 to 0.1 kHz with E_{dc} = 0 V, E_{ac} as 10 mV at an open-circuit potential. Based on this EIS analysis, all modified electrodes exhibit different diameters of a semicircle in the high-frequency region corresponding to charge transfer resistance at the interface of the electrode/electrolyte (R_2). The value of R_2 can be calculated by fitting the obtained Nyquist plots of four electrodes with Randle's equivalent circuit as shown in the inset of Figure 4b. From the EIS analysis, the R_2 values of bare SPCE, SPCE-A800, SPCE-A600, and SPCE-A400 were calculated as 388, 350, 344, and 299 Ω, respectively. The lowest value of resistance was obtained at SPCE-A400, indicating the highest conductivity among the other electrodes. This phenomenon can be explained by the smaller length-to-width ratio and higher crystallinity of AuNR particles, which create a well-packed structure and thus reduce charge transfer resistance on the electrode surface. This well-packed structure of AuNR particles could facilitate better electron transfer phenomena and increase the surface area when the electrode was modified with A400. In addition, the largest surface area of A400 on the electrode surface has been confirmed by another instrumental technique such as AFM, as indicated by its surface roughness. This will eventually enhance the current response of SPCE-A400 that promises a better electrochemical response compared to other electrodes.

The electrochemical active surface area (ECSA) is an important parameter to investigate the effect of the aspect ratio of AuNR on the electrochemical performance of the modified electrodes. ECSA was evaluated by measuring 1 mM $K_3[Fe(CN)_6]$ in 0.1 M KCl using the CV technique at a scan rate ranging from 25 to 150 mV s^{-1} using four different electrodes (bare SPCE, SPCE-A400, SPCE-A600, SPCE-A800) as depicted in Figure 4c–f. Based on the inset of these figures, the current intensity of the redox pair (oxidation and reduction) of $K_3[Fe(CN)_6]$ linearly increases with the square root of the scan rate at four different electrodes. These results indicated that electrochemical redox processes that occur on the surface of the modified electrode are kinetically

https://doi.org/10.1021/acsomega.3c07831
ACS Omega 2024, 9, 1497−1515

Table 1. Interference Effect and Recovery Value for the Determination of 100 μM Carbaryl in the Presence of Several Interfering Species

electrodes	interferences	level of interference ratio (interference/carbaryl)	$j_{carbaryl}$ (μA cm^{-2})	recovery (%)
SPCE-A400			18.18 ± 0.08	
	$NaNO_2$	1:1	18.14 ± 0.06	99.67
	NH_4NO_3	1:1	18.19 ± 0.12	100.08
	$Zn(CH_3CO_2)_2$	1:1	18.49 ± 0.20	102.53
	$FeSO_4$	1:1	18.14 ± 0.19	100.03
	diazinon	1:1	18.25 ± 0.08	100.60
	glucose	1:1	18.07 ± 0.19	99.37
SPCE-A600			16.22 ± 0.13	
	$NaNO_2$	1:1	16.19 ± 0.23	99.67
	NH_4NO_3	1:1	16.19 ± 0.23	99.77
	$Zn(CH_3CO_2)_2$	1:1	16.35 ± 0.13	101.45
	$FeSO_4$	1:1	16.09 ± 0.15	99.11
	diazinon	1:1	16.23 ± 0.16	100.20
	glucose	1:1	16.20 ± 0.16	100.08
SPCE-A800			15.30 ± 0.17	
	$NaNO_2$	1:1	15.07 ± 0.10	97.57
	NH_4NO_3	1:1	15.26 ± 0.18	99.56
	$Zn(CH_3CO_2)_2$	1:1	15.00 ± 0.10	96.86
	$FeSO_4$	1:1	15.05 ± 0.03	99.79
	diazinon	1:1	15.07 ± 0.03	97.65
	glucose	1:1	14.98 ± 0.07	99.07

Table 2. Determination of Carbaryl Concentration in Vegetable Samples Using Three Types of SPCE-Modified AuNRs Using a Standard Addition Technique

sample	electrode	amount added (μM)	amount found (μM)	recovery (%)	RSD (%)
cabbage	SPCE-A400	15	14.64	102.21 ± 2.72	3.44
		25	27.06	101.22 ± 3.20	3.63
		35	34.33	99.69 ± 2.86	2.72
	SPCE-A600	15	14.45	97.24 ± 3.19	3.29
		25	24.24	99.16 ± 3.25	3.63
		35	35.22	98.68 ± 2.91	3.52
	SPCE-A800	15	15.51	103.69 ± 3.89	2.05
		25	23.95	96.23 ± 1.29	4.50
		35	36.06	102.87 ± 4.27	1.95
cucumber	SPCE-A400	15	15.18	98.52 ± 3.42	4.28
		25	24.22	99.41 ± 3.65	2.25
		35	35.30	103.60 ± 3.67	2.72
	SPCE-A600	15	15.25	98.39 ± 3.29	1.00
		25	25.87	107.39 ± 3.49	1.69
		35	34.93	108.14 ± 3.62	3.12
	SPCE-A800	15	14.89	101.60 ± 4.38	2.32
		25	26.07	95.57 ± 3.26	2.51
		35	35.94	97.65 ± 4.31	3.55
Chinese cabbage	SPCE-A400	15	15.74	109.28 ± 3.69	2.62
		25	26.93	102.63 ± 5.25	3.95
		35	35.41	99.34 ± 3.75	3.71
	SPCE-A600	15	14.45	106.60 ± 3.69	4.54
		25	26.31	104.99 ± 3.50	2.20
		35	35.32	104.80 ± 4.68	1.44
	SPCE-A800	15	15.44	103.31 ± 4.17	1.33
		25	26.11	97.56 ± 4.13	1.47
		35	33.96	104.11 ± 5.12	2.01

controlled by diffusion phenomena. The ECSA values of four different electrodes can be calculated using the Randles–Sevcik equation as follows

$$I_p = 2.69 \times 10^5 n^{3/2} D^{1/2} A C v^{1/2}$$

where n = 1 is the number of electrons transferred during the redox reaction of $[Fe(CN)_6]^{3-/4-}$, $D = 6.70 \times 10^{-6}$ cm^2 s^{-1} is the diffusion coefficient of $[Fe(CN)_6]^{3-/4-}$ as previously reported in ref 89, A is the effective area of modified electrode (cm^2), v is the scan rate during the investigation of $[Fe(CN)_6]^{3-/4-}$ species, and C is the concentration of $K_3[Fe(CN)_6]$ used in the measurements (mol cm^{-3}). Based on this equation, it can be determined that the electrochemical active surface area (ECSA) values for bare SPCE, SPCE-A400, SPCE-A600, and SPCE-A800 are 0.0591, 0.6685, 0.5503, and 0.4866 cm^2, respectively. This result indicates that the smaller AuNR aspect ratio provides a higher electrochemical active surface area on the modified electrode, thus resulting in an enhanced electrocatalytic activity compared to other electrodes including bare SPCE. In addition, the modification of AuNRs with different aspect ratios on the surface of bare SPCE could accelerate the electron transfer process in the redox reaction of $[Fe(CN)_6]^{3-/4-}$ species indicated by a smaller difference between oxidation and reduction potential (ΔE). Therefore, it is expected that SPCE-AuNR400 will provide the highest electrocatalytic activity toward carbaryl detection among other electrodes.

Electrochemical Behavior of Carbaryl Detection Using Three Types of SPCE-Modified AuNRs. Carbaryl is difficult to detect by the voltammetry technique due to the lower electroactivity of the amide group in neutral pH, and thus its direct electrochemical measurement is not feasible. Therefore, in this study, carbaryl was hydrolyzed into 1-naphthol in alkaline conditions, specifically above pH 9.[90] The role of the AuNR aspect ratio toward carbaryl detection was investigated using the CV technique by measuring hydrolyzed carbaryl in 0.1 M phosphate buffer of pH 4 using four different electrodes (bare SPCE, SPCE-A400, SPCE-A600, and SPCE-A800). Figure 5a shows the voltammograms at a scan rate of 100 mV s^{-1} obtained from four different electrodes in 0.1 M phosphate buffer of pH 4 containing 100 μM carbaryl. From this figure, an obvious enhancement of the oxidation peak of carbaryl occurred for all modified electrodes. In addition, it can be seen that all electrodes based on SPCE-modified AuNRs show a higher current intensity of carbaryl oxidation compared to bare SPCE. This result confirms that the AuNR structure can enhance the electrocatalytic activity toward carbaryl oxidation. As seen in the inset of Figure 5a, the current intensity of carbaryl oxidation can be calculated as follows 2.12, 3.79, 3.87, and 4.59 μA for bare SPCE, SPCE-A800, SPCE-A600, SPCE-A400, respectively. The highest current of carbaryl oxidation was shown at SPCE-A400, consistent with the obtained result from the electrochemical measurements of the $[Fe(CN)_6]^{3-/4-}$ redox species. The enhancement of current intensity found in AuNR-based electrodes might be due to the presence of surface facets of AuNR increasing a larger electrochemically active area and role as active sites during the electrocatalytic oxidation of carbaryl. The important parameters to investigate the electrochemical sensing performance of carbaryl by AuNR-based electrodes will be elucidated in further experiments.

https://doi.org/10.1021/acsomega.3c07831
ACS Omega 2024, 9, 1497−1515

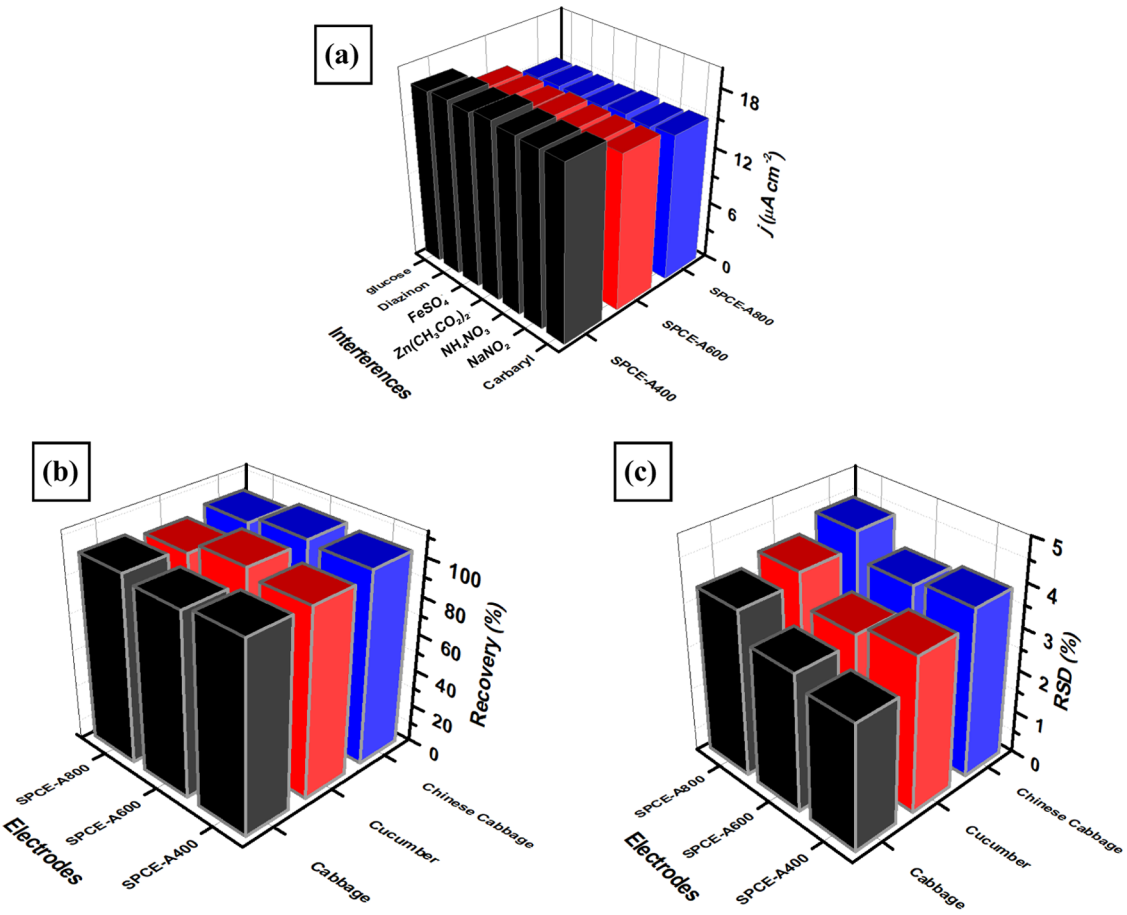

Figure 10. (a) Current response of three types of SPCE-modified AuNRs for the measurements of 100 μM carbaryl in the presence of several interfering species (glucose, diazinon, $FeSO_4$, $Zn(CH_3CO_2)_2$, NH_4NO_3, $NaNO_2$) in the concentration ratio of 1:1, the values of (b) average recovery and (c) relative standard deviation (RSD) obtained from the measurement of carbaryl concentration in three different samples (cabbage, cucumber, and Chinese cabbage) using three types of SPCE-modified AuNRs.

Table 3. Comparison of the Electroanalytical Performance of the Proposed Carbaryl Sensors with Several Previous Sensors

technique	electrode	linear range (μM)	LOD (μM)	sample	ref
CV, DPV	$ZnCo_2O_4$/SPCE	0.15−100	0.05	tomatoes, grapes, and cabbages	93
CV, DPV	Bio-Ag/ZnO/SPCE	0.25−100	0.27	cabbages	94
amperometric	PANI/CoAl-LDH[c]/GCE	0.1−150	0.0068	cucumber, spinach	90
amperometric	MAPDIA[a]-GCE	0.0035−13.96	0.0011	tap water	96
CV, DPV	rGO/AuNPs/SPCE	0.5−250	0.2	tap and river water	97
CV, DPV	LSX zeolite-CPE[b]	1−100	0.3	tomato	98
CV	PPy-IC-DS1-AuNP-AChE[d]	0.05−0.25	0.033	tap water	99
CV, DPV	3D graphene-AuNPs/GCE	0.004−0.3	0.0012	peach, apple, grape, tomato, cucumber, water	100
CV, DPV	rGO/Cu/CuO-Ag/GCE	0.05−20	0.005	grape, orange, tomato, cabbages	101
CV, DPV	carbon black-SPCE	0.1−100	0.048	durum wheat, organic	102
CV, DPV	poly-*p*-phenylenediamine-ionic liquid-CPE	0.5−200	0.09	spring water, grapes	103
CV, DPV	AuNRs in three different aspect ratios/SPCE	0.2−100	0.07	cabbage, cucumber, Chinese cabbage	this work

[a]5-[(4-(Methacryloyloxy)phenyl)diazenyl]isophthalic acid. [b]Low silica *X* zeolite-carbon paste electrode. [c]Polyaniline-layered double hydroxide. [d]Polypyrrole-indigocarmine-dodecylsulfate-AuNPs-acetylcholinesterase.

Effect of pH in the Electrocatalytic Oxidation of Carbaryl Using Three Types of SPCE-Modified AuNRs. The effect of electrolyte pH in the electrocatalytic oxidation of carbaryl was studied by employing the DPV technique using three different modified electrodes (SPCE-A400, SPCE-A600, and SPCE-A800). Figure 5b shows the obtained voltammogram of 0.1 M phosphate buffer of pH 4 containing 100 μM hydrolyzed carbaryl at a scan rate of 50 mV s^{-1} in the pH range from 3 to 6 in triplicate experiments. It can be seen from this figure that the current peak of carbaryl oxidation greatly enhanced toward pH values from 3 to 4 and gradually decreased at pH values 5 and 6. The highest current intensity of carbaryl oxidation was obtained at pH 4. Therefore, pH 4 was chosen as the optimum pH and selected for further studies to investigate the electrocatalytic oxidation of carbaryls using modified electrodes. In addition, Figure 5c displays the linear relationship between the pH of carbaryl solution versus its oxidation potential with the equation: E_{pa} (V) = −0.0495*x* +

https://doi.org/10.1021/acsomega.3c07831
ACS Omega 2024, 9, 1497−1515

0.3785 (R^2 = 0.98). It is clear that the peak of oxidation potentials (E_{pa}) slightly shifted toward more positive potential, corresponding to the increasing pH of carbaryl solution. In addition, the slope of linear regression is −0.0495 V/pH that is close to the theoretical value of Nernst constant $\left(-\frac{0.059m}{n}\right)$ V/pH where n and m are the number of transferred electrons and protons involving in the electrocatalytic process of carbaryl oxidation. As a result, it can be considered that one proton and one electron participated in the electrocatalytic oxidation of carbaryls on the surface of modified electrodes. The slight difference between the slope value with Nernst constant might be due to the fact that the number of protons and electrons involved in the carbaryl oxidation was not completely identical (the ratio between the n/m value was estimated at nearly 1.19). This indicates the irreversibility of the carbaryl peak during the process of electrocatalytic oxidation and will be discussed in the next section about the effect of scan rate.

Evaluation of the Effect of Scan Rate in the Electrocatalytic Oxidation of Carbaryl Using Three Types of SPCE-Modified AuNRs. The effect of scan rate on the electrocatalytic oxidation of carbaryl using three modified electrodes was investigated by measuring 100 μM carbaryl in 0.1 M phosphate buffer of pH 4 at various scan rates (10−250 mV s^{-1}). As illustrated in Figure 6a,c,e, three modified electrodes (SPCE-A400, SPCE-A600, and SPCE-A800) exhibit the increases in the anodic peak current of carbaryl oxidation corresponding to the increase of scan rates from 10 to 250 mV s^{-1}. From these investigations, three linear regressions related to each modified electrode can be obtained as follows

SPCE-A400: I_p (μA)
$= 7.4653\ (\text{mV s}^{-1})^{1/2} + 1.2299;\ R^2$
$= 0.9933$

SPCE-A600: I_p (μA)
$= 6.238\ (\text{mV s}^{-1})^{1/2} + 0.1351;\ R^2$
$= 0.9972$

SPCE-A800: I_p (μA)
$= 5.5921\ (\text{mV s}^{-1})^{1/2} + 0.2418;\ R^2$
$= 0.9982$

Thus, it can be inferred from all of these linear regressions that the process of carbaryl oxidation at the surface of modified electrodes was preferably controlled by diffusion phenomena. In a further study of the scan rate effect, the potential peak of carbaryl oxidation (E_{pa}) increased linearly with the natural logarithm of the scan rate (ln v) at various scan rates. There are three linear regressions obtained from this investigation, as displayed in Figure 6b,d,f, based on the following equations

SPCE-A400: E_{pa} (V)
$= 0.0404 \ln v\ (\text{V s}^{-1}) + 0.5527;\ R^2$
$= 0.9966$

SPCE-A600: E_{pa} (V)
$= 0.0384 \ln v\ (\text{V s}^{-1}) + 0.5468;\ R^2$
$= 0.9936$

SPCE-A800: E_{pa} (μA)
$= 0.0334 \ln v\ (\text{V s}^{-1}) + 0.5301;\ R^2$
$= 0.9914$

Based on Laviron's theory for the irreversible process of electron transfer on the electrode surface, the relationship between the anodic peak potential (E_{pa}) versus the scan rate (v) can be expressed in the following equation

$$E_{pa} = E_o + \left(\frac{RT}{(1-\alpha)nF}\right)\ln\left(\frac{(1-\alpha)nF}{RTk_{et}}\right) + \left(\frac{RT}{(1-\alpha)nF}\right)\ln v$$

It can be deduced from the equation above that the slope of the regression equation is equal to $RT/(1-\alpha)nF$, where T is the absolute temperature (298 K), R is the gas constant (8.314 J mol^{-1} K^{-1}), and F is the Faraday constant (96485.33 C mol^{-1}), n is the number of transferred electrons, α is the electron transfer coefficient, and k_{et} is the electron transfer constant. The number of electrons involved in the electrocatalytic oxidation of carbaryl at three different SPCE-modified AuNRs can be determined using the following equation with α assumed as 0.5

$$E_{pa} = E_o + \frac{RT}{(1-\alpha)nF}\ln v$$

From the predetermined slope values (ln v vs E_{pa}) of each modified electrode, the values for n during the carbaryl oxidation could be determined as 1 with the corresponding electron transfer coefficient (α) found as 0.36, 0.33, and 0.23 for SPCE-A400, SPCE-A600, and SPCE-A800. Notably, the electron transfer rate constant (k_{et}) can be calculated using the following equation based on Laviron's theory[91,92]

$$k_{et} = \frac{\alpha nFv_c}{RT}$$

where α, n, F, R, and T have similar meanings, and v_c is the selected scan rate (0.05 V s^{-1}). Based on this equation, the values of k_{et} for SPCE-A400, SPCE-A600, and SPCE-A800 were calculated to be 0.701, 0.642, and 0.447 s^{-1}, respectively. Therefore, SPCE-A400 displayed the highest electron transfer rate constant (k_{et}) showing faster electron transfer due to high electron conduction compared to other modified electrodes. In addition, the surface coverage for each modified electrode can be determined based on its adsorption capacity of carbaryl on the electrode surface following the below equation

$$I_p = n^2F^2Av\Gamma/4RT$$

where n is the number of transferred electrons during carbaryl oxidation, F is the Faraday constant (C mol^{-1}), A is the surface area of the modified electrode (cm^2), Γ is the surface coverage of the modified electrode (mol cm^{-2}), v is the scan rate (V s^{-1}), R is the universal gas constant (J K^{-1} mol^{-1}), and T is the absolute temperature (K). The absorption capacity of each modified electrode can be calculated from the values of the

https://doi.org/10.1021/acsomega.3c07831
ACS Omega 2024, 9, 1497−1515

observed slope of I_{pa} versus v for SPCE-A400, SPCE-A600, and SPCE-A800 being 3.18×10^{-5}, 2.2×10^{-5}, and 1.22×10^{-5} mol cm^{-2}, respectively. In comparison, previous works have determined the value of adsorption capacity of electrochemical sensors based on modified electrodes for carbaryl detection and obtained comparable results with our work.[93,94] Based on these results, it can be concluded that the modified electrodes based on SPCE-modified AuNR400 displayed the largest capacity for carbaryl adsorption on the electrode surface among other developed electrodes.

Chronoamperometry Studies Using Three Types of SPCE-Modified AuNRs to Investigate the Electrocatalytic Oxidation of Carbaryl. A chronoamperometry study was employed to investigate the performance of all three modified electrodes for the electrocatalytic oxidation of carbaryl. The experiment of chronoamperometry study was performed in the range of carbaryl concentration from 20 to 100 μM in 0.1 M phosphate buffer of pH 4 using three types of modified electrodes (SPCE-A400, SPCE-A600, and SPCE-A400). As displayed in Figure 7a,c,e, all amperometric responses from three modified electrodes indicate that an increase of carbaryl concentration in a concentration range from 20 to 100 μM corresponds to the increasing anodic current of carbaryl oxidation. From this study, the diffusion coefficient from each modified electrode can be calculated using the Cottrell equation

$$I = nFACD^{1/2}\pi^{1/2}t^{-1/2}$$

where n is the number of electrons participating in the carbaryl oxidation that was obtained from Laviron studies in the previous sections (1), D is the diffusion coefficient of carbaryl (cm^2 s^{-1}), C is the bulk concentration of carbaryl (mol cm^{-3}), and A is the area of the electrode (0.07 cm^2). It can be seen from the inset of Figure 7a,c,e that all plots of I versus $t^{-1/2}$ obtained from all modified electrodes showed a linear relationship with the calculated D values for SPCE-A400, SPCE-A600, and SPCE-A800 were 1.7×10^{-5}, 1.6×10^{-5}, and 1.5×10^{-5} cm^2 s^{-1}, respectively. From this investigation, it can be concluded that SPCE-A400 shows the highest value for the diffusion coefficient among the other electrodes. Figure 7b,d,f displays three calibration plots corresponding to the response of the chronoamperometry study performed using all modified electrodes at different concentrations of carbaryl.

In addition, the catalytic rate constant of each modified electrode can be obtained by plotting the linear relationship between the current intensity (I) and the square root of time ($t^{1/2}$). Three calibration plots of I versus $t^{1/2}$ were derived with the equations: $I_{cat}/I_L = 1.0173t^{1/2} + 0.6712$ ($R^2 = 0.9938$) for SPCE-A400, $I_{cat}/I_L = 0.6649t^{1/2} + 0.7397$ ($R^2 = 0.9906$) for SPCE-A600, and $I_{cat}/I_L = 0.5677t^{1/2} + 0.9392$ ($R^2 = 0.9873$) for SPCE-A800. Then, the catalytic rate constant (k_{cat}) can be determined using Galus method following the equation

$$I_{cat}/I_L = (\pi t)^{1/2}(k_{cat}C_0)^{1/2}$$

where I_{cat} is the catalytic current of carbaryl measured with SPCE-A400, SPCE-A600, or SPCE-A800, I_L is the finite current without carbaryl, k_{cat} is the catalytic rate constant (cm^3 mol^{-1} s^{-1}), C_0 is the carbaryl concentration, and t is the time (s). Thus, according to the slopes of I_{cat}/I_L versus $t^{1/2}$, the calculated k_{cat} values are 5.49×10^6 for SPCE-A400, 2.34×10^6 for SPCE-A600, and 1.71×10^6 for SPCE-A800. It can be deduced that the obtained catalytic rate constant (k_{cat}) for SPCE-AuNR400 is the highest compared to other electrodes, which can be attributed to the higher electron transfer rate of SPCE-A400.

Electroanalytical Performance of Three Types of SPCE-Modified AuNRs for Carbaryl Detection. The electroanalytical performance of three types of modified electrodes (SPCE-A400, SPCE-AR600, and SPCE-A800) was investigated by using the DPV technique to obtain several optimum parameters such as linearity, limit of detection (LOD), and limit of quantification (LOQ). The DPV technique was employed for the measurements of 0.1 M phosphate buffer of pH 4 containing different concentrations of carbaryl from 0.2 to 100 μM. Based on Figure 8a–c, the anodic peak currents can be observed on all modified electrodes linearly increasing with the increase of carbaryl concentrations to yield three calibration plots as shown in the inset of Figure 8a–c. The corresponding calibration plots found in three modified electrodes are I_{pa} (μA) = $0.1174C_{carbaryl}$ (μM) + 6.7014 (R^2 = 0.9960, 0.2–100 μM) for SPCE-A400, I_{pa} (μA) = $0.0973C_{carbaryl}$ (μM) + 6.5791 (R^2 = 0.9965, 0.6–100 μM) for SPCE-A600, and I_{pa} (μA) = $0.0883C_{carbaryl}$ (μM) + 6.2706 (R^2 = 0.9976, 1–100 μM) for SPCE-A800. Thus, the limit of detection (LOD) (S/N) and limit of quantification (LOQ) of three modified electrodes can be consecutively calculated for SPCE-A400 as 0.07 and 0.2 μM, for SPCE-A600 as 0.1 and 0.6 μM, and for SPCE-A800 as 0.5 and 1 μM. In addition, the electrochemical sensitivity can be determined from the slope of the calibration curve with the lowest value obtained as 6.54 μA μM^{-1} cm^{-2} for SPCE-A400 compared to 2.85 μA μM^{-1} cm^{-2} for SPCE-A600 and 1.01 μA μM^{-1} cm^{-2} for SPCE-A800. In summary, SPCE-A400 achieved superior analytical performance in terms of higher sensitivity with lower LOD and LOQ over a wider linear range for carbaryl detection compared to SPCE-A600 and SPCE-A800.

The mechanism of carbaryl oxidation on the surface of SPCE-modified AuNRs can be deduced following the two processes: (1) the hydrolysis of carbaryl molecules into 1-naphthol in an alkaline condition and (2) the oxidation of hydroxyl (OH^-) functional groups within the 1-naphthol chemical structure by removing 1 electron and 1 proton (H^+) with the corresponding anodic oxidation peak at 0.2 V. The mechanism of carbaryl oxidation at the surface of SPCE-modified AuNR is illustrated in Figure 8d. Furthermore, recent studies demonstrated the oxidation of 1-naphthol using SPCE-modified metal nanoparticles, and the metal oxide composite occurs at 0.4 V as reported in ref 93 and at 0.5 V as reported in ref 94. Based on this result, it can be inferred that the SPCE-modified facet-controlled anisotropic gold nanoparticles provide faster electron transfer kinetics to oxidize carbaryl molecules than bare SPCE.

Reproducibility and Selectivity of Three Types of SPCE-Modified AuNRs. The reproducibility of modified electrodes (SPCE-A400, SPCE-A600, and SPCE-A800) was evaluated by measuring 100 μM carbaryl in 0.1 M phosphate buffer of pH 4 using six electrodes for each modification. The experiments of measuring carbaryl concentration using each electrode were performed in triplicate experiments using DPV techniques at a scan rate of 50 mV s^{-1}. The values of relative standard deviation from this investigation for each modified electrode of SPCE-A400, SPCE-A600, and SPCE-A800 were 1.57, 1.73, and 2.47%, respectively, as shown in Figure 9a. Meanwhile, when the stability measurements of three types of modified electrodes were performed by measuring 100 μM

https://doi.org/10.1021/acsomega.3c07831
ACS Omega 2024, 9, 1497–1515

carbaryl in 0.1 M phosphate buffer of pH 4 in 4 consecutive days, it was found that the anodic current of carbaryl oxidation was dropped down after 3 days. This is due to the fact that the molecule product of carbaryl oxidation might be adsorbed on the electrode surface and start to poison the electrocatalytic activity of AuNR-based electrodes. Therefore, these three modified electrodes might be suitable for further development as disposable electrochemical sensors. In addition, the selectivity of three types of modified electrodes was evaluated by measuring 100 μM carbaryl in the presence of several interfering species such as inorganic compounds and another type of insecticide. The selected interferences for this selectivity study were $NaNO_2$, NH_4NO_3, $Zn(CH_3CO_2)_2$, $FeSO_4$, diazinon, and glucose in a concentration of 100 μM and mixed with 100 μM carbaryl. As displayed in Figure 9b−d, the response current from all three types of modified electrodes shows a negligible influence (the value of standard error less than 0.2%) when several interference species were added and measured at the oxidation potential of carbaryl at 0.2 V. These results reveal that all modified electrodes display an exceptional selectivity toward carbaryl oxidation and almost no effect from interfering species. Further evaluation from this selectivity investigation is the value of standard deviation (RSD) in the range of 96−102% (Table 1) and shows the acceptance in analytical range.[95]

Real Sample Analysis Using Three Types of SPCE-Modified AuNRs. The performance of three types of SPCE-modified AuNRs for practical applications in carbaryl detection was evaluated for real samples (cabbage, cucumber, Chinese cabbage) using a standard addition technique. Three levels of carbaryl concentrations were added to real samples and analyzed with the DPV technique under optimum conditions. The real concentration of carbaryl in the samples was then determined using the regression equation of standard calibration curve derived from three types of SPCE-modified AuNRs as summarized in Table 2. It was found that the average recovery value for SPCE-modified A400 from the range 96−103% with the average relative standard deviation (RSD) for three levels of added carbaryl concentration is 3.26% (n = 3). In addition, based on Figure 10a−c, the average recoveries for SPCE-A600 and SPCE-A800 were in the range of 96−100% (%RSD = 3.48%) and 95−103% (%RSD = 2.85%), respectively. Moreover, the comparison of the electroanalytical performance of our proposed sensors for carbaryl detection with several previously reported sensors is also summarized in Table 3.

This proposed sensor showed a lower limit of detection compared to other previously reported sensors for carbaryl detection.[13,97,98,103] Furthermore, several platform types for carbaryl detection displayed a lower limit of detection[96,100] due to higher conductivity of the platform materials. Nevertheless, this proposed sensor exhibited a wider linear range of carbaryl detection compared to other modified electrodes.[99,101,102] The advantage of this proposed sensor for carbaryl detection includes a lower limit of detection and a wider linear range of concentration that could be attributed to the electrocatalytic activity of gold nanorod-modified SPCE. Based on this result, it can be inferred that SPCE-modified AuNR provides analytical performance comparable to that of previous sensors and good reliability for monitoring carbaryl concentration in the selected sample of vegetables.

CONCLUSIONS

In this work, we have demonstrated the feasibility of an electrochemical sensing strategy for carbaryl detection using a commercial screen-printed carbon electrode (SPCE) modified with different aspect ratios of gold nanorods (AuNRs). Gold nanorods were synthesized using seed-growth-mediated methods by varying the amount of $AgNO_3$ (400, 600, and 800 μL) to control the facet growth of Au nanoparticles. The obtained AuNR solutions were then characterized using UV−vis spectroscopy and TEM techniques to accurately determine its aspect ratios, which are 2.21, 2.53, and 2.85, respectively. In addition, the surface of SPCE-modified AuNRs in different aspect ratios was further characterized with SEM, AFM techniques, and EIS studies. Then, the modified electrodes based on the different aspect ratios of AuNRs were employed for carbaryl detection in acidic conditions by converting it first into 1-naphthol that is a more electroactive compound. It was revealed that the smaller aspect ratio of the AuNR-modified SPCE (SPCE-A400) shows the best electrochemical response among other electrodes as a platform for carbaryl sensing. The performance of SPCE-A400 for carbaryl detection has been successfully quantified in a wide linear range of concentration (0.2−100 μM) with a low limit of detection (0.07 μM) and the highest electrochemical sensitivity up to 6.54 $\mu A\ \mu M^{-1}\ cm^{-2}$ compared to other two electrodes. Furthermore, the proposed electrochemical sensor also showed good reproducibility and selectivity among several potential interfering species, although this platform might be more suitable to further develop as a disposable sensor. For practical applications, this proposed sensor can reliably determine the carbaryl concentration in vegetable samples such as cabbage, cucumber, and Chinese cabbage with the average of recovery values of 101, 100.5, and 103.8%, respectively. In summary, this proposed electrochemical sensor based on controlled facets of gold nanorods offers great potential to be employed for monitoring pesticide concentration in the environment. This result is also intriguing to be further explored with other types of electroactive molecules particularly for pollutant compounds.

AUTHOR INFORMATION

Corresponding Author

Wulan Tri Wahyuni − *Analytical Chemistry Division, Department of Chemistry, Faculty of Mathematics and Natural Sciences, Kampus IPB Dramaga, Bogor 16680, Indonesia; Tropical Biopharmaca Research Center, Institute of Research and Community Empowerment, IPB University, Bogor 16680, Indonesia;* orcid.org/0000-0002-3071-4974; Email: wulantriws@apps.ipb.ac.id

Authors

Budi Riza Putra − *Research Center for Metallurgy, National Research and Innovation Agency (BRIN), South Tangerang, Banten 15315, Indonesia*

Hemas Arif Rahman − *Analytical Chemistry Division, Department of Chemistry, Faculty of Mathematics and Natural Sciences, Kampus IPB Dramaga, Bogor 16680, Indonesia*

Tribidasari A. Ivandini − *Department of Chemistry, Faculty of Mathematics and Natural Sciences, University of Indonesia, Depok 16424, Indonesia;* orcid.org/0000-0002-5282-5325

https://doi.org/10.1021/acsomega.3c07831
ACS Omega 2024, 9, 1497−1515

Irkham − *Department of Chemistry, Faculty of Mathematics and Natural Sciences, University of Padjajaran, Bandung 45363, Indonesia;* orcid.org/0000-0001-9938-2931

Munawar Khalil − *Department of Chemistry, Faculty of Mathematics and Natural Sciences, University of Indonesia, Depok 16424, Indonesia;* orcid.org/0000-0002-7712-1738

Isnaini Rahmawati − *Department of Chemistry, Faculty of Mathematics and Natural Sciences, University of Indonesia, Depok 16424, Indonesia*

Complete contact information is available at: https://pubs.acs.org/10.1021/acsomega.3c07831

Notes

The authors declare no competing financial interest.

■ ACKNOWLEDGMENTS

The authors acknowledge Riset Kolaborasi Indonesia PTNBH with contract number 17198/IT3.D10/PT.01.02/P/T/2023 fiscal year 2023 for the research funding.

■ REFERENCES

(1) Zhang, Y.; Zheng, Q.; Chen, X.; Guan, Y.; Dai, J.; Zhang, M.; Dong, Y.; Tan, H. Comparison and analysis of several quantitative identification models of pesticide residues based on quick detection paperboard. *Processes* **2023**, *11* (6), 1854.

(2) Thorat, T.; Patle, B. K.; Wakchaure, M.; Parihar, L. Advancements in techniques used for identification of pesticide residue on crops. *J. Nat. Pest. Res.* **2023**, *4*, No. 100031.

(3) Végh, R.; Csoka, M.; Mednyanszky, Z.; Sipos, L. Pesticide residues in bee bread, propolis, beeswax and royal jelly- A review of the literature and dietary risk assessment. *Food Chem. Toxicol.* **2023**, *176*, No. 113806.

(4) Sindhu, S.; Manickavasagan, A. Nondestructive testing methods for pesticide residue in food commodities: A review. *Compr. Rev. Food Sci. Food Saf.* **2023**, *22* (2), 1226−1256.

(5) Wang, Q.; Yang, D.; Rui, C.; Zhou, L.; Li, R.; Wang, L.; Huang, W.; Ji, X.; Yang, Q.; Liang, P.; Yuan, H.; Cui, L. Seed treatment with chlorantraniliprole and carbaryl mixture for managing fall armyworm on maize: systemic synergism, control efficiency and synergistic mechanism. *Pest Manag. Sci.* **2023**, *79* (1), 464−473.

(6) Joshi, R.; Adhikari, S.; Son, J. P.; Jang, Y.; Lee, D.; Choo, B.-K. Au nanogap SERS substrate for the carbaryl pesticide determination in juice and milk using chemometrics. *Spectrochim. Acta, Part A* **2023**, *297*, No. 122734.

(7) Bedrossiantz, J.; Faria, M.; Prats, E.; Barata, C.; Cachot, J.; Raldua, D. Heart rate and behavioral response in three phylogenetically distant aquatic model organisms exposed to environmental concentrations of carbaryl and fenitrothion. *Sci. Total Environ.* **2023**, *865*, No. 161268.

(8) Dinca, V.; Docea, A. O.; Drocas, A. I.; Nikolouzakis, T. K.; Stivaktakis, P. D.; Nikitovic, D.; Golokhvast, K. S.; Hernandez, A. F.; Calina, D.; Tsatsakis, A. A mixture of 13 pesticides, contaminants, and food additives below individual NOAELs produces histopathological and organ weight changes in rats. *Arch. Toxicol.* **2023**, *97*, 1285−1298.

(9) Khatun, P.; Islam, A.; Sachi, S.; Islam, M. Z.; Islam, P. Pesticides in vegetable production in Bangladesh: A systemic review of contamination levels and associated health risks in the last decade. *Toxicol. Rep.* **2023**, *11*, 199−211.

(10) Dorozhko, E. V.; Gashevskay, A. S.; Korotkova, E. I.; Barek, J.; Vyskocil, V.; Eremin, S. A.; Galuni, E. V.; Saqib, M. A copper nanoparticle-based electrochemical immunosensor for carbaryl detection. *Talanta* **2021**, *228*, No. 122174.

(11) Code of Federal Regulations. https://www.ecfr.gov/current/title-40/chapter-I/subchapter-E/part-180/subpart-C/section-180.169 (accessed on Sept 27, 2023).

(12) Hassanzadeh, N.; Bahramifar, N.; Esmaili-Sari, A. Residue content of carbaryl applied on greenhouse cucumbers and its reduction by duration of a pre-harvest interval and post-harvest household processing. *J. Sci. Food Agric.* **2010**, *90*, 2249−2253.

(13) Cuchiaro, J.; Baumgartner, J.; Reynolds, M. M. Modeling a pesticide remediation strategy for preparative liquid chromatography using high-performance liquid chromatography. *J. Cannabis Res.* **2023**, *5*, No. 13.

(14) Farajpour, S.; Mogaddam, M. R. A.; Khandaghi, J. Combination of QuECHERS dispersive liquid-liquid microextraction based on magnetic ionic liquids for extraction of carbamate pesticides from apple samples prior to their analysis by high performance liquid chromatography. *J. Food. Technol. Nutr.* **2023**, *20*, 5−16.

(15) Chen, T.; Zhu, R.; Zhang, W.; Li, J.; Qiu, G.; Wu, F.; Xu, Y.; Chen, M.; Qi, P. High-throughput screening and quantification of pesticides in Lili Bulbus by ultra-performance liquid chromatography coupled with quadrupole-time of flight mass spectrometry. *Anal. Methods* **2023**, 5466−5473, DOI: 10.1039/D3AY01212C.

(16) Yao, B.; Li, Y.; Zhang, R.; Yao, L.; Xu, J.; Yan, C.; Chen, W. Simultaneous determination of 6 carbamate pesticides and relevant metabolites in oilseeds and oil with the modified fast QuECHERS method by ultra-performance liquid chromatography-tandem mass spectrometry. *J. Future Foods* **2024**, *4* (1), 97−104.

(17) Yang, B.; Wang, S.; Ma, W.; Li, G.; Tu, M.; Ma, Z.; Zhang, Q.; Li, H.; Li, X. Simultaneous determination of neonicotinoid and carbamate pesticides in freeze-dried cabbage by modified QuECHERS and ultra-performance liquid chromatography-tandem mass spectrometry. *Foods* **2023**, *12* (4), 699.

(18) Shi, Y.; Jin, H.-F.; Shi, M.-Z.; Cao, J.; Ye, L.-H. Carbon black-assisted miniaturized solid-phase extraction of carbamate residues from ginger by supercritical fluid chromatography combined with ion mobility quadrupole time-of-flight mass spectrometry. *Microchem. J.* **2023**, *194*, No. 109335.

(19) Louati, K.; Kolsi, F.; Kallel, R.; Gdoura, Y.; Borni, M.; Hakim, L. S.; Zribi, R.; Choura, S.; Maalej, A.; Sayadi, S.; Chamkha, M.; Mnif, B.; Khemakhem, Z.; Boudawara, T. S.; Boudawara, M. Z.; Safta, F. Research of pesticide metabolites in human brain tumor tissues by chemometrics-based gas chromatography-mass spectrometry analysis for a hypothetical correlation between pesticide exposure and risk factor of central nervous system tumors. *ACS Omega* **2023**, *8* (32), 29812−29835.

(20) Kim, H.; Baek, E. J.; Kim, Y.-K.; Park, H.; Hur, S. H.; Kim, J.-E.; Kim, H. J. Development of a method for analysis and risk assessment of residual pesticides in ginseng using liquid and gas chromatography-tandem mass spectrometry. *Food Chem.* **2023**, *427*, No. 136675.

(21) Guo, Z.; Wu, X.; Jayan, H.; Yin, L.; Xue, S.; El-Seedi, H. R.; Zou, X. Recent developments and applications of surface enhanced Raman scattering spectroscopy of fruits and vegetables. *Food Chem.* **2024**, *434*, No. 137469.

(22) Lin, S.; Fang, X.; Fang, G.; Liu, F.; Dong, H.; Zhao, H.; Zhang, J.; Dong, B. Ultrasensitive detection and distinction of pollutants based on SERS assisted by machine learning algorithms. *Sens. Actuators, B* **2023**, *384*, No. 133651.

(23) Villanueva, E.; Glorio-Paulet, P.; Giusti, M. M.; Sigurdson, G. T.; Yao, S.; Rodriguez-Saona, L. E. Screening for pesticide residues in cocoa (*Theobroma cacao* L.) by portable infrared spectroscopy. *Talanta* **2023**, *257*, No. 124386.

(24) Raja, D. A.; Rahim, S.; Shah, M. R.; Bhanger, M. I.; Malik, M. I. Silver nanoparticle based efficient colorimetric assay for carbaryl − An insecticide. *J. Mol. Liq.* **2023**, *372*, No. 121200.

(25) Hao, H.; Zhu, J.; Yang, B.; Peng, L.; Lou, S. Ovalbumin-coated gold nanoparticles with interesting colloidal stability for colorimetric detection of carbaryl in complex media. *Food Chem.* **2023**, *403*, No. 134485.

(26) Feng, J.; Gong, Y.; Yang, S.; Tian, H.; Sun, B. A colorimetric fluorescent probe for the detection of carboxylesterase and carbamate pesticides. *Anal. Sci.* **2023**, *39*, 1909−1916, DOI: 10.1007/s44211-023-00398-2.

(27) Yang, Y.; Tong, C.; Zhou, R.; Qin, Z.; Xu, J.; Liao, C.; Zhang, S.; Shi, S.; Guo, Y. Hinge-like paper-based dual-channel enzyme-free ratiometric fluorescent microfluidic platform for simultaneous visual detection of carbaryl and glyphosate. *Food Chem.* **2024**, *431*, No. 137127.
(28) Han, X.; Liu, C.; Guo, X.; Sui, J.; Lin, H.; Chen, X.; Cao, L. Controlling the amount of coupling agents on the synthesis of coating antigens to enhance the sensitivity of fluoroquinolone immunodetection. *Heliyon* **2023**, *9*, No. e16821.
(29) Liu, M.-l.; Chen, Z.-J.; Huang, X.-q.; Wang, H.; Zhao, J.-l.; Shen, Y.-d.; Luo, L.; Wen, Xw.; Hammock, B.; Xu, Z. l. A bispecific nanobody with high sensitivity/efficiency for simultaneous determination of carbaryl and its metabolite 1-naphthol in the soil and rice samples. *Environ. Pollut.* **2023**, *335*, No. 122265.
(30) Kunpatee, K.; Kalcher, K.; Chailapakul, O.; Chaiyo, S.; Samphao, A. A paper chromatographic-based electrochemical analytical device for the separation and simultaneous detection of carbofuran and carbaryl pesticides. *Sens. Actuators, B* **2023**, *377*, No. 133116.
(31) Amatatongchai, M.; Thimoonnee, S.; Somnet, K.; Chairam, S.; Jarujamrus, P.; Nacapricha, D.; Lieberzeit, P. A. Origami 3D-microfluidic paper-based analytical device for detecting carbaryl using mesoporous silica-platinum nanoparticles with a molecularly imprinted polymer shell. *Talanta* **2023**, *254*, No. 124202.
(32) Saqib, M.; Solomonenko, A. N.; Barek, J.; Dorozhko, E. I.; Korotkova, E. I.; Aljasar, S. A. Graphene derivatives-based electrodes for the electrochemical determination of carbamate pesticides in food products: A review. *Anal. Chim. Acta* **2023**, *1272*, No. 341449.
(33) Feng, J.; Gong, Y.; Bai, Y.; Yang, S.; Tian, H.; Sun, B. A fluorescent benzothiazole probe for the detection of carboxylesterase and carbamate pesticides. *ChemistrySelect* **2023**, *8* (36), No. e202303160.
(34) Zhu, L.; Wu, M.; Li, R.; Zhao, Y.; Lu, Y.; Wang, T.; Du, L.; Wan, L. Research progress on pesticide residue detection based on microfluidic technology. *Electrophoresis* **2023**, *44* (17−18), 1377−1404.
(35) Toth, J.; Pineda, M.; Yargeau, V. Fast and simplified quantitative multiresidue analytical method for pesticide in surface waters by UHPLC-MS/MS with online sample preparation. *Chemosphere* **2023**, *318*, No. 137962.
(36) Ta'alia, S. A. H.; Rohaeti, E.; Putra, B. R.; Wahyuni, W. T. Electrochemical sensors for simultaneous detection of dopamine and uric acid based on a composite of electrochemically reduced graphene oxide and PEDOT:PSS-modified glassy carbon electrode. *Results Chem.* **2023**, *6*, No. 101024.
(37) Rahman, H. A.; Rafi, M.; Putra, B. R.; Wahyuni, W. T. Electrochemical sensors based on a composite of electrochemically reduced graphene oxide and PEDOT:PSS for hydrazine detection. *ACS Omega* **2023**, *8* (3), 3258−3269.
(38) Silva, R. M.; da Silva, A. D.; Camargo, J. R.; de Castro, B. S.; Meireles, L. M.; Silva, P. S.; Janegitz, B. C.; Silva, T. A. Carbon nanomaterials-based screen-printed electrodes for sensing applications. *Biosensors* **2023**, *13* (4), 453.
(39) Atici, T.; Kamac, M. B.; Yilmaz, M.; Kabaca, A. Y. Zinc oxide nanorod/polymethylene blue (deep eutectic solvent)/gold nanoparticles modified electrode for electrochemical determination of serotonin (5HT). *Electrochim. Acta* **2023**, *458*, No. 142484.
(40) Ouedraogo, B.; Baachaoui, S.; Tall, A.; Tapsoba, I.; Raouafi, N. Laser-induced graphene electrodes on polyimide membranes modified with gold nanoparticles for the simultaneous detection of dopamine and uric acid in human serum. *Microchim. Acta* **2023**, *190*, 316.
(41) Kader, M. A.; Azmi, N. S.; Kafi, A. K. M. Recent advances in gold nanoparticles modified electrodes in electrochemical non-enzymatic sensing of chemical and biological compound. *Inorg. Chem. Commun.* **2023**, *153*, No. 110767.
(42) Ma, X.; Zhang, H.; Liu, J.; Zhang, H.; Hu, X.; Wang, Y.; Li, X.; Xu, J. An ultrahigh-resolution multicolor sensing platform via target-induced etching of gold nanorods for multi-colorimetric analysis of trace silver ions. *Sens. Actuators, B* **2023**, *397*, No. 134658.
(43) Lang, Q.; Han, L.; Haou, C.; Wang, F.; Liu, A. A sensitive acetylcholinesterase biosensor based on gold nanorods modified electrode for detection of organophosphate pesticide. *Talanta* **2016**, *156−157*, 34−41.
(44) Liu, Y.; Lv, B.; Liu, A.; Liang, G.; Yin, L.; Pu, Y.; Wei, W.; Gou, S.; Liu, S. Multicolor sensor for organophosphorus pesticides determination based on the bi-enzyme catalytic etching of gold nanorods. *Sens. Actuators, B* **2018**, *265*, 675−681.
(45) Hashkavayi, A. B.; Raoof, J. B.; Ojani, R.; Asl, E. H. Label-free electrochemical aptasensor for determination chloramphenicol based on gold nanocubes-modified screen-printed gold electrode. *Electroanalysis* **2015**, *27* (6), 1449−1456.
(46) Shahid, M. M.; Rameshkumar, P.; Basirunc, W. J.; Wijayantha, U.; Chiu, W. S.; Khiew, P. S.; Huang, N. M. An electrochemical sensing platform of cobalt oxide@gold nanocubes interleaved reduced graphene oxide for the selective determination of hydrazine. *Electrochim. Acta* **2018**, *259*, 606−616.
(47) Manickam, P.; Vashist, A.; Madhu, S.; Sadasivam, M.; Sakthivel, A.; Kaushik, A.; Nair, M. Gold nanocubes embedded biocompatible hybrid hydrogels for electrochemical detection of H_2O_2. *Bioelectrochemistry* **2020**, *131*, No. 107373.
(48) Wang, P.; Chen, S.; Guan, Y.; Li, Y.; Jiamali, A. An electrochemical sensing platform based on gold nanostars for the detection of Alzheimer's disease marker Aβ oligomers (Aβo). *Alex. Eng. J.* **2023**, *81*, 1−6.
(49) Schuck, A.; Kim, H. E.; Kang, M.; Kim, Y.-S. Gold nanostar-modified electrochemical sensor for highly sensitive renin quantification as a marker of tissue-perfusion. *MRS Commun.* **2023**, *13*, 1150−1155, DOI: 10.1557/s43579-023-00414-6.
(50) Khosravi, F.; Rahaie, M.; Ghaani, M. R.; Azimzadeh, M.; Mostafavi, E. Ultrasensitive electrochemical miR-155 nanocomposite biosensor based on functionalized/conjugated graphene materials and gold nanostars. *Sens. Actuators, B* **2023**, *375*, No. 132877.
(51) Xiao, W.; Xiong, Y.; Li, Y.; Chen, Z.; Li, H. Non-enzymatically colorimetric bilirubin sensing based on the catalytic structure disruption of gold nanocages. *Sensors* **2023**, *23* (6), 2969.
(52) Aliakbarpour, S.; Amjadi, M.; Hallaj, T. A colorimetric assay for H_2O_2 and glucose based on the morphology transformation of Au/Ag nanocages to nanoboxes. *Food Chem.* **2024**, *432*, No. 137273.
(53) Yao, Y.; Wang, G.; Chu, G.; An, X.; Guo, Y.; Sun, X. The development of a novel biosensor based on gold nanocages/graphene oxide-chitosan modified acetylcholinesterase for organophosphorus pesticide detection. *New J. Chem.* **2019**, *43*, 13816−13826.
(54) Liu, H.-L.; Ahmed, S. A.; Jiang, Q.-C.; Shen, Q.; Zhan, K.; Wang, K. Gold nanotriangle-assembled nanoporous structures for electric field-assisted surface-enhanced Raman scattering detection of adenosine triphosphate. *ACS Sens.* **2023**, *8* (3), 1280−1286.
(55) Chavez, M.; Fernandez-Merino, A.; del Cano, R.; Sanchez-Obrero, G.; Madueno, R.; Blazquez, M.; Pineda, T. Behind the optimization of the sensor film: bioconjugation of the triangular gold nanoparticles with hemoproteins for sensitivity enhancement of enzymatic biosensors. *Biosensors* **2023**, *13* (4), 467.
(56) Li, H.; Geng, W.; Zheng, Z.; Haruna, S. A.; Chen, Q. Flexible SERS sensor using AuNTs-assembled PDMS film coupled chemometric algorithms for rapid detection of chloramphenicol in food. *Food Chem.* **2023**, *418*, No. 135998.
(57) Wang, Y.; Zhang, Y.; Du, Q.; Cao, D.; Lu, X.; Meng, Z. Sensitive SERS detection of oral squamous cell carcinoma-related miRNAs in saliva via a gold nanohexagon array coupled with hybridization chain reaction amplification. *Anal. Methods* **2022**, *14*, 4563−4575.
(58) Manikandan, M.; Abdelhamid, H. N.; Talib, A.; Wu, H.-F. Facile synthesis of gold nanohexagons on graphene templates in Raman spectroscopy for biosensing cancer and cancer stem cells. *Biosens. Bioelectrons.* **2014**, *55*, 180−186.
(59) Singh, P.; Ahn, S.; Kang, J.-P.; Veronika, S.; Huo, Y.; Singh, H.; Chokkaligam, M.; Farh, M. E.-A.; Aceituno, V. C. *In vitro* anti-

https://doi.org/10.1021/acsomega.3c07831
ACS Omega 2024, 9, 1497−1515

inflammatory activity of spherical silver nanoparticles and monodisperse hexagonal gold nanoparticles by fruit extract of *Prunus serrulate*: a green synthetic approach. *Artif. Cells Nanomed. Biotechnol.* **2018**, *46* (8), 2022−2032.
(60) Mei, X.; Wang, W.; Li, Q.; Wu, M.; Bu, L.; Chen, Z. A novel electrochemical sensor based on gold nanobipyramids and poly-L-cysteine for sensitive determination of trilobatin. *Analyst* **2023**, *148*, 2335−2342.
(61) Nafisah, S.; Morsin, M.; Iwantono, I.; Sanudin, R.; Zain, Z. M.; Satria, L.; Razali, N. L.; Mardiansyah, D. Growth time dependency on the formation of gold bipyramids for efficient detection towards chlorpyrifos-based LSPR sensor. *Optik* **2023**, *289*, No. 171270.
(62) Jiang, W.; Sun, D.; Cai, C.; Zhang, H. Sensitive detection of extracellular hydrogen peroxide using plasmon-enhanced electrochemical activity on Pd-tipped Au nanobipyramids. *Analyst* **2023**, *148*, 3791−3797.
(63) Zheng, J.; Cheng, X.; Zhang, H.; Bai, X.; Ai, R.; Shao, L.; Wang, J. Gold nanorods: The most versatile plasmonic nanoparticles. *Chem. Rev.* **2021**, *121* (21), 13342−13453.
(64) Zhou, C.; Liu, D.; Xu, L.; Li, Q.; Song, J.; Xu, S.; Xing, R.; Song, H. A sensitive label-free amperometric immunosensor for alpha-fetoprotein based on gold nanorods with different aspect ratio. *Sci. Rep.* **2015**, *5*, No. 9939.
(65) Dai, Y.; He, G.; Long, S.; Li, X.; Meng, L.; Wang, P.; Li, X.; Yang, Z. Precise tailoring of mesoporous silica-coated gold nanorods for laser ignition of 1064 nm. *ACS Appl. Nano Mater.* **2023**, *6*, 4946−4956.
(66) Safitri, H.; Wahyuni, W. T.; Rohaeti, E.; Khalil, M.; Marken, F. Optimization of uric acid detection with Au nanorod-decorated graphene oxide (GO/AuNR) using response surface methodology. *RSC Adv.* **2022**, *12*, 25269−25278.
(67) Yang, S.; Cheng, Y.; Cheng, D.; Wang, Y.; Xu, H.; Li, M.; Jiang, T.; Wang, H. N-doped graphene-supported gold nanorods for electrochemical sensing of ascorbic acid with superior sensitivity. *J. Electron. Mater.* **2023**, *52*, 2336−2346.
(68) Govindasamy, M.; Manavalan, S.; Chen, S.-M.; Rajaji, U.; Chen, T.-W.; Al-Hemaid, F. M. A.; Ali, M. A.; Elsikh, M. S. Determination of neurotransmitter in biological and drug samples using gold nanorods decorated *f*-MWCNTs modified electrode. *J. Electrochem. Soc.* **2018**, *165*, B370.
(69) Sabahat, S.; Ejaz, M.; Saira, F.; Saleem, R. S. Z.; Nazish, Y.; Khalil, L.; Naeem, A. Surface plasmon resonance-based synthesis of gold nanorods for sensing applications. *Chem. Pap.* **2023**, *77*, 5901−5911.
(70) Datta, D.; Lim, J. W.; Maji, R. C.; Maji, S. K. Graphene oxide-wrapped gold nanorods for direct plasmon-enhanced electrocatalysis to detect hydrogen peroxide and in the hydrogen evaluation reaction. *ACS Appl. Nano Mater.* **2023**, *6* (4), 2729−2740.
(71) Li, H.; Huang, T.; Yuan, H.; Lu, L.; Cao, Z.; Zhang, L.; Yang, Y.; Yu, B.; Wang, H. Combined ultrasensitive detection of renal cancer proteins and cells using an optical microfiber functionalized with Ti_3C_2 MXene and gold nanorod-sensitized interfaces. *Anal. Chem.* **2023**, *95* (11), 5142−5150.
(72) Husna, R.; Kurup, C. K.; Ansari, M. A.; Mohd-Naim, N. F.; Ahmed, M. U. An electrochemical aptasensor based on AuNRs/AuNWs for sensitive detection of apolipoprotein A-1 (ApoA1) from human serum. *RSC Adv.* **2023**, *13*, 3890−3898.
(73) Tang, C.; Wang, A.-J.; Feng, J.-J.; Cheang, T. Y. Mulberry-like porous-hollow AuPtAg nanorods for electrochemical immunosensing of biomarker myoglobin. *Microchim. Acta* **2023**, *190*, No. 233.
(74) Nguyen, M. T. T.; Dang, L. T.; Pham, H. V. Gold nanorods coated by molecularly imprinted polymer for sensitive and specific SERS detection of dyes. *Colloid Polym. Sci.* **2023**, *301*, 577−586.
(75) Deng, K.; Li, C.; Li, X.; Huang, H. Simultaneous detection of sunset yellow and tartrazine using the nanohybrid of gold nanorods decorated graphene oxide. *J. Electroanal. Chem.* **2016**, *780*, 296−302.
(76) Han, E.; Li, X.; Zhang, Y.; Zhang, M.; Cai, J.; Zhang, X. Electrochemical immunosensor based on self-assembled gold nanorods for label-free and sensitive determination of *Staphylococcus aureus*. *Anal. Biochem.* **2020**, *611*, No. 113982.
(77) Mahari, S.; Roberts, A.; Gandhi, S. Probe-free nanosensor for the detection of *Salmonella* using gold nanorods as an electroactive modulator. *Food Chem.* **2022**, *390*, No. 133219.
(78) Murillo Pulgarín, J. A.; Bermejo, L. F. G.; Duran, A. C. Simultaneous chemiluminescent determination of carbaryl and 1-naphthol in soils using a flow-injection system. *Int. J. Environ. Anal. Chem.* **2018**, *98* (2), 111−123.
(79) Hawker, D. Kinetics of carbaryl hydrolysis: An undergraduate environmental chemistry laboratory. *J. Chem. Educ.* **2015**, *92* (9), 1531−1525.
(80) Gou, L.; Murphy, C. J. Fine-tuning the shape of gold nanorods. *Chem. Mater.* **2005**, *17*, 3668−3672.
(81) Chankhunthod, N.; Kidkhunthod, P. Synthesis of tunable near infrared absorbance of gold nanorods (AuNRs) and their gold oxidation states during nanorod formation following by synchrotron based X-ray absorption spectroscopy (XANES). *Radiat. Phys. Chem.* **2023**, *207*, No. 110844.
(82) Nikoobakht, B.; El-Sayed, M. A. Preparation and growth mechanism of gold nanorods (NRs) using seed-mediated growth method. *Chem. Mater.* **2003**, *15* (10), 1957−1962.
(83) Liu, M.; Guyot-Sionnest, P. Mechanism of silver(I)-assisted growth of gold nanorod and bipyramids. *J. Phys. Chem. C* **2005**, *109* (47), 22192−22200.
(84) Dreaden, E. C.; Alkilany, A. M.; Huang, X.; Murphy, C. J.; El-Sayed, M. A. The golden age: gold nanoparticles for biomedicine. *Chem. Soc. Rev.* **2012**, *41*, 2740−2779.
(85) Park, K.; Drummy, L. F.; Wadams, R. C.; Koemer, H.; Nepal, D.; Fabris, L.; Vaia, R. A. Growth mechanism of gold nanorods. *Chem. Mater.* **2013**, *25* (4), 555−563.
(86) Chirea, M.; Cruz, A.; Pereira, C. M.; Silva, A. F. Size-dependent electrochemical properties of gold nanorods. *J. Phys. Chem. C* **2009**, *113*, 13077−13087.
(87) Wadams, R. C.; Fabris, L.; Vaia, R. A.; Park, K. Time-dependent susceptibility of the growth of gold nanorods to the addition of a cosurfactant. *Chem. Mater.* **2013**, *25* (23), 4772−4780.
(88) Nehru, R.; Gnanakrishnan, S.; Chen, C.-W.; Dong, C.-D. Nanoscale Mn_3O_4 electrocatalyst as improved electrode materials for electrochemical sensing of chloramphenicol drugs. *ACS Appl. Nano. Mater.* **2023**, *6* (2), 1235−1249.
(89) Feng, J.; Lang, G.; Li, T.; Zhang, J.; Zhao, J.; Li, W.; Yang, W.; Jiang, Z. Enhanced electrochemical detection of C-Cr_2O_3 towards glucose and hydrazine by assembling Ni-MPN coating. *Appl. Suf. Sci.* **2022**, *604*, No. 154548.
(90) Jiao, W.; Ding, G.; Wang, L.; Liu, Y.; Zhan, T. Polyaniline functionalized CoAl-layered double hydroxide nanosheets as a platform for the electrochemical detection of carbaryl and isoprocarb. *Microchim. Acta* **2022**, *189*, No. 78.
(91) Lang, J.; Wang, W.; Zhou, Y.; Guo, D.; Shi, R.; Zhou, N. Electrochemical behavior and direct quantitative determination of paclitaxel. *Front. Chem.* **2022**, *10*, No. 834154.
(92) Amudi, K.; Yigit, A.; Menges, N.; Pinar, P. T. Highly selective electrochemical sensor for new generation targeted-anticancer drug Ibrutinib using newly synthesized nanomaterial GO-NH-N$(OH)_2$@AgNPs modified glassy carbon electrode. *Measurement.* **2023**, *216*, No. 112978.
(93) Huyen, N. N.; Tung, L. M.; Nguyen, T. A.; Phung, T. L. H.; Thang, P. D.; Vinh, N. T.; Nguyen, Q. V.; Vu, T. K. O.; Lam, V. D.; Le, V. K.; Dinh, N. X.; Le, A.-T. Insights into the effect of cation distribution at tetrahedral sites in $ZnCo_2O_4$ spinel nanostructures on the charge transfer ability and electrocatalytic activity toward ultrasensitive detection of carbaryl pesticide in fruit and vegetable samples. *J. Phys. Chem. C* **2023**, *127*, 12262−12275.
(94) Le Nhat Trang, N.; Nga, D. T. N.; Tufa, L. T.; Tran, V. T.; Hung, T.-T.; Phan, V. N.; Pham, T. N.; Hoang, V.-T.; Le, A.-T. Unveiling the effect of crystallinity and particle size of biogenic Ag/ZnO nanocomposites on the electrochemical sensing performance of

https://doi.org/10.1021/acsomega.3c07831
ACS Omega 2024, 9, 1497−1515

carbaryl detection in agricultural products. *RSC Adv.* **2023**, *13*, 8753−8764.
(95) Della Pelle, F.; Angelini, C.; Sergi, M.; Carlo, M. D.; Pepe, A.; Compagnone, D. Nano carbon black-based screen printed sensor for carbofuran, isoprocarb, carbaryl, and fenobucarb detection: application to grain samples. *Talanta* **2018**, *186*, 389−396.
(96) Liu, L.; Ding, Z.; Tan, Y.; Yi, Y.; Liao, S.; Wang, D.; Ye, Q.; Zeng, C.; Tan, N. A kind of new type photoresponsive molecularly imprinted electrochemical sensor based on 5-[(4-methacryloyloxy)-phenyl)diazenyla]isopthalic acid for the detection of carbaryl. *J. Sol. State Electrochem.* **2023**, *27*, 301−312.
(97) Albalawi, I.; Alatawi, H.; Alseri, S.; Moore, E. Electrochemical synthesis of reduced graphene oxide/gold nanoparticles in a single step for carbaryl detection. *Sensors* **2022**, *22*, No. 5251.
(98) Salih, F. E.; Achiou, B.; Ouammou, M.; Bennazha, J.; Ouarzane, A.; Younssi, S. A.; Rhazi, M. E. Electrochemical sensor based on low silica X zeolite modified carbon paste for carbaryl determination. *J. Adv. Res.* **2017**, *8* (6), 669−676.
(99) Loguercio, L. F.; Thesing, A.; Demingos, P.; de Albuquerque, C. D. L.; Rodrigues, R. S. B.; Brolo, A. G.; Santos, J. F. L. Efficient acetylcholinesterase immobilization for improved electrochemical performance in polypyrrole nanocomposite-based biosensors for carbaryl pesticide. *Sens. Actuators, B* **2021**, *339*, No. 129875.
(100) Rahmani, T.; Bagheri, H.; Behbahani, M.; Hajian, A.; Afkhami, A. Modified 3D graphene-Au as a novel sensing layer for direct and sensitive electrochemical determination of carbaryl pesticide in fruit vegetable, and water samples. *Food Anal. Methods* **2018**, *11*, 3005−3014.
(101) Hashemi, P.; Karimian, N.; Khoshsafar, H.; Arduini, F.; Mesri, M.; Afkhami, A.; Bagheri, H. Reduced graphene oxide decorated on Cu/CuO-Ag nanocomposite as a high-performance material for the construction of a non-enzymatic sensor: Application to the determination of carbaryl and fenamiphos pesticides. *Mater. Sci. Eng. C* **2019**, *102*, 764−772.
(102) Della Pelle, F.; Angelini, C.; Sergi, M.; Carlo, M. D.; Pepe, A.; Compagnone, D. Nano carbon black-based screen printed sensor for carbofuran, isoprocarb, carbaryl and fenobucarb detection: application to grain samples. *Talanta* **2018**, *186*, 389−396.
(103) Salih, F. E.; Oularbi, L.; Halim, E.; Elbasri, M.; Ouarzane, A.; Rhazi, M. E. Conducting polymer/ionic liquid composite modified carbon paste electrode for the determination of carbaryl in real samples. *Electroanalysis* **2018**, *30*, 1855−1864.

https://doi.org/10.1021/acsomega.3c07831
ACS Omega 2024, 9, 1497−1515